Cell Reports

Resource

Organelle proteomics of human, neonatal pig, healthy and diabetic mouse islets

Graphical abstract

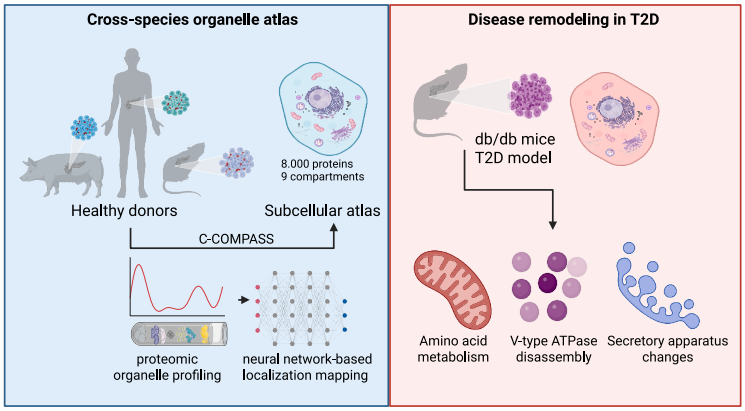

Authors

Özüm Sehnaz Caliskan, Daniel Thomas Haas, Joana Verissimo Ferreira, ..., Heiko Lickert, Mostafa Bakhti, Natalie Krahmer

Correspondence

natalie.krahmer@helmholtz-munich.de

In brief

Caliskan, Haas et al. present a cross-species subcellular proteomic atlas of pancreatic islets, revealing conserved organelle organization across human, pig, and mouse. The study uncovers disease-associated remodeling of vesicular trafficking, granule acidification machinery, and mitochondrial metabolism in a mouse model of type 2 diabetes.

Highlights

- Cross-species islet atlas maps conserved cytoarchitecture and insulin granule proteome
- Phosphoinositide signaling and vesicular trafficking reorganize in T2D
- Insulin granule acidification machinery disassembles in T2D
- Mitochondria upregulate proline synthesis in T2D

Caliskan et al., 2026, Cell Reports *45*, 117751
August 25, 2026
https://doi.org/10.1016/j.celrep.2026.117751

CellPress

Cell Reports

CellPress
OPEN ACCESS

Resource

Organelle proteomics of human, neonatal pig, healthy and diabetic mouse islets

Özüm Sehnaz Caliskan,[1,2,8] Daniel Thomas Haas,[1,2,8] Joana Verissimo Ferreira,[1,2] Sabina Chubanava,[1,2] Elisabeth Kemter,[2,3,4] Perla Cota,[2,5] Aimée Bastidas-Ponce,[2,5] Marta Tarquis-Medina,[2,5] Oliver Czarnecki,[2,5] Sreya Bhattacharya,[2,5] Jessica Jaki,[2,5] Verena Geiger,[2,5] Pamela Kakimoto,[1,2] Daniel Brandt,[1,2] Magdalena Sachser,[2,3,4] Carina Dürr,[1,2] Hilda Delgado de la Herran,[1,2] Alberto Cebrian-Serrano,[1,2] Timo Dirk Müller,[1,2,6] Eckhard Wolf,[2,3,4] Heiko Lickert,[2,5] Mostafa Bakhti,[2,5] and Natalie Krahmer[1,2,7,9,*]

[1]Institute for Diabetes and Obesity, Helmholtz Munich, Neuherberg, Germany
[2]German Center for Diabetes Research (DZD), Neuherberg, Germany
[3]Institute of Molecular Animal Breeding and Biotechnology, Gene Center and Department of Veterinary Sciences, Ludwig-Maximilians-Universität Munich, Munich, Germany
[4]Center for Innovative Medical Models (CiMM), Ludwig-Maximilians-Universität Munich, Oberschleissheim, Germany
[5]Institute of Diabetes and Regeneration Research, Helmholtz Munich, Neuherberg, Germany
[6]Walther-Straub-Institute for Pharmacology and Toxicology, Ludwig-Maximilians-Universität Munich, Munich, Germany
[7]Metabolic Cell Architecture, Department of Molecular Life Sciences, TUM School of Life Sciences, Technical University of Munich, Munich, Germany
[8]These authors contributed equally
[9]Lead contact
*Correspondence: natalie.krahmer@helmholtz-munich.de
https://doi.org/10.1016/j.celrep.2026.117751

SUMMARY

Pancreatic islets, in which β cells constitute 50%–80% of the endocrine mass, are the body's site for glucose-regulated insulin secretion. Pancreatic islet dysfunction is a hallmark of type 2 diabetes. Nevertheless, the molecular changes that impair their function remain insufficiently understood. To determine how islet cellular organization supports function and how it deteriorates in disease, we used machine learning-based organelle proteomics to build an organelle atlas of pancreatic islets from mice, humans, and pig neonatal islet-like cells. This cross-species resource maps localization of ∼8,000 proteins, revealing conserved organelle organization and identifying previously unrecognized components of insulin granules. Applying our organelle proteomics workflow to db/db mice, a T2D model uncovered disease-associated changes affecting vesicular trafficking and mitochondrial amino acid metabolism. Additionally, we found a disassembly of the insulin-granule acidification machinery. Our atlas provides insights into islet subcellular organization and identifies processes whose disruption may drive pancreatic islet failure in T2D.

INTRODUCTION

Pancreatic islets are the main regulators of whole-body glucose balance, and their impairment is a hallmark of type 2 diabetes (T2D). In mammals, β cells make up 50%–80% of the islet tissue mass. These cells detect circulating glucose and nutrient levels and respond with tightly regulated insulin secretion to keep blood glucose within a narrow range. The β cells work together with glucagon-producing α cells and somatostatin-producing δ cells to fine-tune glycemic control,[1] with glucagon stimulating insulin secretion and somatostatin suppressing it.[2]

The endocrine cell types of pancreatic islets, their roles, and regulatory pathways are conserved across mammals. However, mice and pigs, two species commonly used for research and xenotransplantation, display species-specific differences in islet structure and function compared with humans. In both pigs and humans, fetal islets first form a mantle-core structure but undergo gestational remodeling into an intermingled α-/β-cell arrangement.[3] Mice are reported to retain the mantle-core architecture throughout life.[4,5] Still, some studies indicate that this canonical core-mantle structure is most evident in young lean animals but can become disrupted with aging or metabolic stress, such as high-fat diet-induced obesity, leading to greater mixing of α and δ cells into the β-cell core.[6,7] Mouse islets also show a higher proportion of β cells, distinct paracrine regulation, and two insulin isoforms.[4,8] In contrast, pigs exhibit a more dispersed endocrine cell organization, stronger islet vascularization, and glucose responsiveness, insulin secretion dynamics, and gene expression patterns more similar to those of human islets.[4,5]

Despite these differences, the core β-cell machinery for insulin secretion is conserved across species. Glucose uptake and oxidative metabolism raise the cytosolic ATP/ADP ratio, closing ATP-sensitive K^+ (KATP) channels,[9] depolarizing the membrane, and activating voltage-dependent Ca^{2+} channels

(VDCCs). The resulting Ca^{2+} influx triggers exocytosis of insulin-containing granules in two phases, a rapid first phase followed by a longer second one, acting on distinct vesicle pools.[10] This specialized endocrine function of β cells depends on their highly organized subcellular structure. Each cell contains about 10,000 insulin granules[11] and a network of organelles specialized to support insulin synthesis, storage, and secretion.[12] The endoplasmic reticulum (ER) and Golgi apparatus are optimized for producing, folding, and packaging bulk cargo into secretory vesicles,[13] while mitochondria have a particularly high capacity for ATP generation to fuel glucose-stimulated insulin secretion.[14] The specialized cytoskeleton coordinates the movement of insulin granules to specific microdomains at the plasma membrane (PM),[15] where KATP and VDCC channels are densely located for glucose sensing and insulin release.[16] At the same time, lysosomes and autophagosomes coordinate proteostasis by degrading misfolded insulin and recycling granule components.[17] This coordination among specialized organelles and the dynamic subcellular organization of β cells allows the maintenance of glucose homeostasis under changing physiological conditions.

Failure of β cells is a defining feature of pancreatic islet dysfunction in T2D,[18] whose prevalence has reached epidemic levels.[19] In the early stages of T2D, β cells initially increase insulin secretion to compensate for systemic insulin resistance, the reduced ability of tissues to respond to insulin under conditions of overnutrition and obesity.[20] However, this compensatory response cannot be sustained in the long term, eventually leading to impaired insulin release, β-cell apoptosis, and chronic hyperglycemia.[21] Despite extensive research on pancreatic dysfunction, including identification of defects in β-cell glucose sensing,[22] insulin secretion pathways,[23] ER stress responses,[24,25] and mitochondrial dysfunction,[26] the underlying molecular processes remain only partly understood.

Single-cell transcriptomics and proteomics allow high-throughput characterization and provide information on the states of individual cell types; however, they do not resolve subcellular organization. Organelle proteomics can address this by capturing subcellular architecture, but it requires large amounts of fresh material and has therefore been applied mainly to highly proliferative cell lines[27–39] or to tissues with large biomass, such as liver.[40,41] These material constraints have limited its use for organs, tissues, or sorted cell populations where only small input amounts are available. Here, we apply organelle proteomics to analyze pancreatic islets, a relatively low-abundance tissue, using a protein correlation profiling (PCP) workflow optimized for reduced protein input at the whole-tissue level. With this approach, we generated a proteomic atlas of pancreatic islet organelles containing localization information for more than 8,000 proteins.

By comparing islet organization across mice, pigs, and humans, and by examining alterations in a T2D mouse model, we characterize pancreatic islet cellular organization and identify disease-related changes in organelle proteomes. Together, this resource provides a cross-species atlas for studying pancreatic islet cell organization and offers insight into the molecular alterations underlying islet dysfunction in T2D.

RESULTS

A cross-species cellular atlas of pancreatic islets

Preclinical endocrine research predominantly uses rodent models due to limited access to human pancreatic tissue. However, the anatomical and physiological differences between rodents and humans can reduce the translational relevance of findings. Pigs provide an alternative, as their pancreatic islet tissue organization and function more closely resemble humans, making them particularly interesting for islet xenotransplantation research.[42] To enable cross-species comparisons of islet cellular organization across the three species, we generated a proteomic cellular atlas of pancreatic islets from healthy young human donors and mice and compared it with a subcellular map of *in vitro* matured pig neonatal islet-like cells (NICCs or NPIs). NICCs were selected rather than adult pig islets because they are easier to isolate, yield substantially more material, and typically show superior survival and functional performance, including robust insulin secretion.[43,44] Our NICC preparations, isolated at postnatal day 3–5 and matured for 8–13 days, showed robust insulin secretion after forskolin stimulation, similar to previously reported NICC responsiveness[45] (Figure S1A), confirming their functionality. As expected from their higher proportions of ductal and progenitor cells, NICCs contained a lower β-cell fraction (~30%) compared with human and mouse islets, which typically contain 50%–70% and 70%–90% β cells, respectively[5] (Figure S1B). To establish a basis for interpreting cross-species differences in subcellular protein localization, we systematically quantified cell composition and maturation markers in the total proteomes (Table S1). Using cell type-specific marker panels,[46] we confirmed that pig NICCs exhibit higher levels of immature β-cell markers compared with mouse islets (Figure S1C). As expected, classical β-cell marker proteins were most abundant in mice, intermediate in humans, and lowest in pig NICCs (Figure S1D), whereas α-cell marker levels were reduced in mice relative to the other species (Figure S1E). Somatostatin levels indicated comparable δ-cell abundance across all three species (Figure S1F). Although the differences in cell-type marker abundance were modest, the comparatively low β-cell content of pig NICCs, and the highest levels observed in mice, should be considered when evaluating cross-species proteomic differences. Some of the observed variations may reflect underlying differences in islet cellular composition rather than exclusively species-specific proteomic features.

Using sucrose density gradients, we separated organelles from the three pancreatic islet models. For mice, islets from five wild type (WT, C57BLKS/J) male mice were pooled per gradient, yielding ~150–200 islet equivalents (IEQs) (~200 μg protein), so the mouse atlas generated from three replicates reflects material from 15 animals. For pig NICCs, we used 20% from each of four independent isolations (two male and two female donors), resulting in ~500 μg protein and ~1,000–1,200 IEQs per gradient; the pig atlas therefore represents tissue from 16 pigs. Human islets from young healthy male donors provided 8,000–12,000 IEQs and 200–500 μg protein per gradient (see Methods for donor characteristics), and due to limited availability of fresh human material in these quantities, the human atlas reflects material from only three donors. The gradients, divided into 24 fractions per sample, were analyzed via liquid

CellPress
OPEN ACCESS

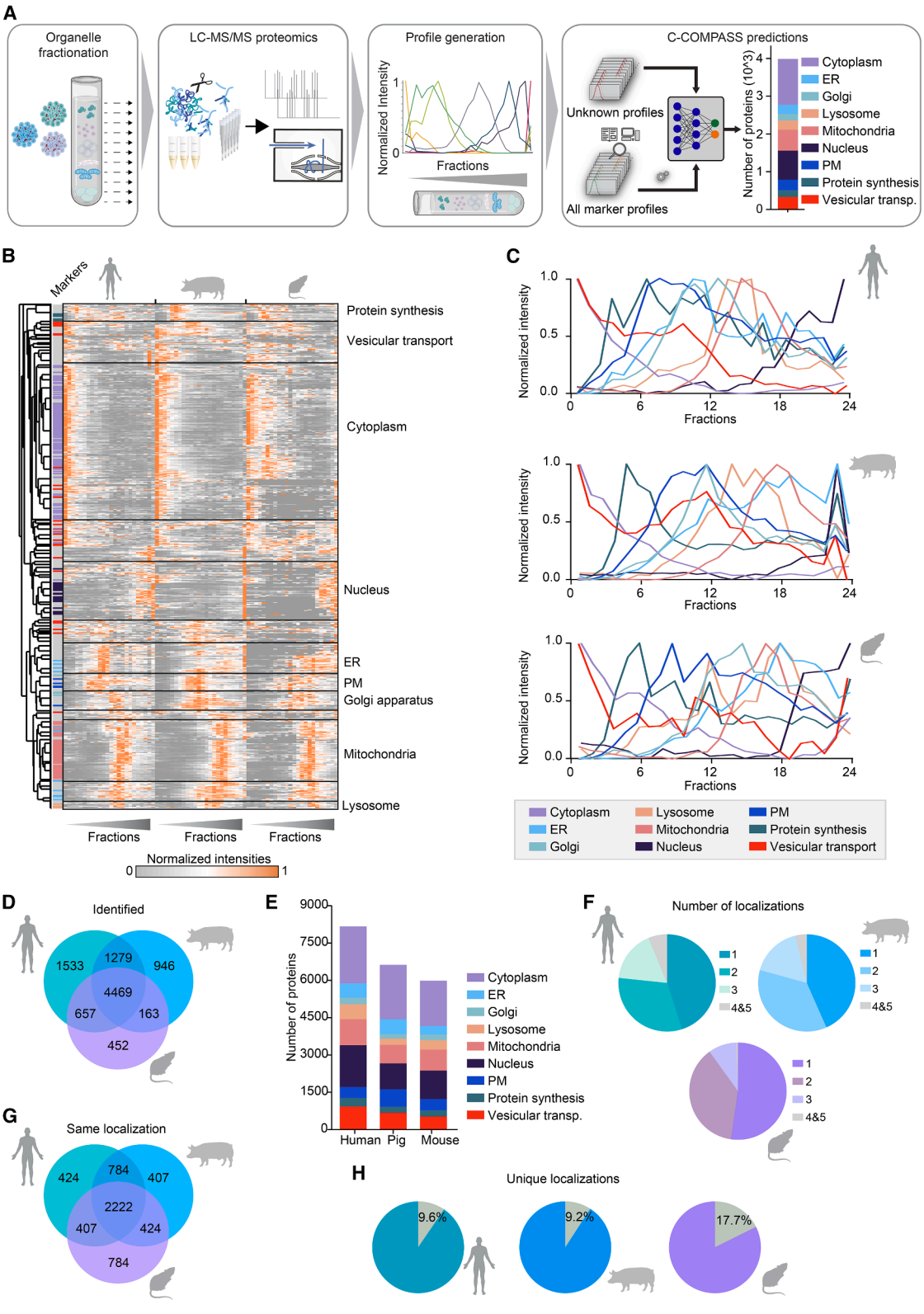

(legend on next page)

chromatography-tandem mass spectrometry (LC-MS/MS) to generate protein abundance profiles for PCP (Figure 1A). PCP enables the systematic mapping of protein localizations without the need for purified organelles, as localizations are inferred by comparing protein fractionation profiles with established organelle markers. First, resolvable compartments were determined through unsupervised hierarchical clustering and enrichment analysis of validated organelle markers derived from the HeLa cell proteomic map[29] and Protein Atlas,[47] which led to the identification of nine compartments with distinct profiles (Figures 1B and 1C; Figure S2A), including major membrane bound compartments and additionally a compartment we named "protein synthesis", which fractionated separately and contained ribosomes and proteins involved in translation. Peroxisomal markers were omitted, and several secretory pathway compartments, such as endosomes or vesicles, were grouped into a single "vesicular transport" category due to resolution limits. Our recently implemented computational tool, C-COMPASS,[48] a machine-learning software using a neural network-based regression model, was then trained on a set of organelle markers for these nine compartments to predict spatial protein distributions of the entire dataset (Table S2).

The organelle maps yielded between 2,023 and 7,748 proteins per fraction (Figure S2B), leading to 7,938 different proteins in total for human islets, 6,857 for pig NICCs, and 5,741 for murine islets. 4,469 proteins were commonly detected across all species (Figure 1D; Table S2). Principal component analysis of all fractions indicated similar separation patterns across species (Figure S2C). The number of organelle classifications and proteins with single and multiple localizations was similar across species (Figures 1E and 1F; Table S3). The accuracy of C-COMPASS assignments exceeded 90% for all compartments; only vesicular trafficking markers displayed lower precision (83.5% for human, 87.5% for pig, and 54.5% for mouse) (Figure S2D). Importantly, while marker profiles for the same compartments were generally very similar across species, minor differences in gradient behavior (Figure S2E) did not compromise the accuracy of C-COMPASS, as the predictions rely on internal comparisons with species-specific markers. Finally, we compared our localization predictions with data from the Human Protein Atlas,[49] which provides immunofluorescence-based localization information from human cell lines. Agreement was high for several organelles such as mitochondria and the nucleus, whereas the overlap in the protein's primary subcellular location was lower for compartments involved in vesicular transport or for the ER. This reduced overlap likely reflects β-cell-specific organizations that are not captured in conventional cell-line models such as U2OS or HeLa cells (Figure S2F).

Species-specific organelle organization and subcellular localization

To assess organelle abundance in pancreatic islets, we integrated the total tissue proteomes with PCP-derived protein localization profiles. Summing the intensities of validated organelle marker proteins across human and mouse islets and pig NICCs enabled estimation of relative organelle abundance and comparison of species-specific cellular organization (Figure S3A). The secretory apparatus components were most abundant in pig NICCs, followed by human islets, whereas mouse islets showed lower levels of involved proteins. This is consistent with the rapid granule turnover and high insulin synthesis rates characteristic of rodent β cells, which maintain smaller storage pools but a highly dynamic secretory apparatus.[50] Mitochondrial proteins were reduced in pig NICCs relative to both mature islet types, aligning with the immature oxidative metabolism reported for NICCs.[51] In contrast, mouse islets had the highest abundance of mitochondrial and protein synthesis machinery, consistent with their high metabolic activity.[52] Lysosomal markers were most abundant in human islets, exceeding levels in both pig NICCs and mouse islets. Together, this indicates distinct organelle profiles across species aligning with their reported metabolic activities and maturation states.

Our pancreatic islet subcellular atlas identified 4,469 proteins shared among islet cells across all three species (Figure 1D), with 2,222 proteins displaying consistent subcellular localization (Figure 1G; Table S4). This subset represents a conserved core proteome, essential for pancreatic islet function, and is enriched in ribosomal proteins, chromatin modifiers, cell cycle regulators, and proteins of essential metabolic pathways. Moreover, we found an enrichment in proteins of compartments requiring specific targeting sequences, particularly those localized to the mitochondria and nucleus (Figure S3B). To explore species-specific differences, we identified proteins with conserved localization in two species but divergent localization in the third. Mouse pancreatic islets exhibited the highest proportion of uniquely localized proteins, with 17.7% showing distinct main organelle classification, compared to 9.2% in pigs and 9.6% in humans (Figure 1H). While some of these variations may stem from species differences, others may reflect differences in isolation protocols, sample handling, maturation state, or cell composition. For example, the distinct localization of developmental regulators, such as the cell-cell adhesion protein and central canonical Wnt signaling transducer β-catenin/CTNNB1 and the Nodal/TGFβ transcription factor SMAD2 in pig NICCs may indicate incomplete maturation (Figures S3C–S3E). Conversely, human islets showed shifts in autophagy related protein profiles compared to mouse and pig and increased co-localization and membrane compartment recruitment of autophagy-related proteins (e.g., ANXA2,

Figure 1. A cross-species proteomic organelle atlas of pancreatic islets

(A) Schematic of organelle proteome mapping by density fractionation, LC-MS/MS, and C-COMPASS neural network-based compartment prediction.
(B) Unsupervised hierarchical clustering of median 0–1 scaled profiles of common proteins across species; enriched organelle markers indicated. (n = 3 human, n = 4 pig, each replicate pooled from two male and two female pigs, n = 3 mouse; each mouse replicate pooled from five male mice).
(C) Median abundance profiles of organelle markers.
(D) Venn diagram of proteins identified per species.
(E) Number of proteins assigned per compartment.
(F) Percentage of proteins with single or multiple compartment assignments.
(G) Venn diagram of overlapping main protein localizations across species.
(H) Proportion of proteins with divergent main organelle assignments between species.

CellPress
OPEN ACCESS

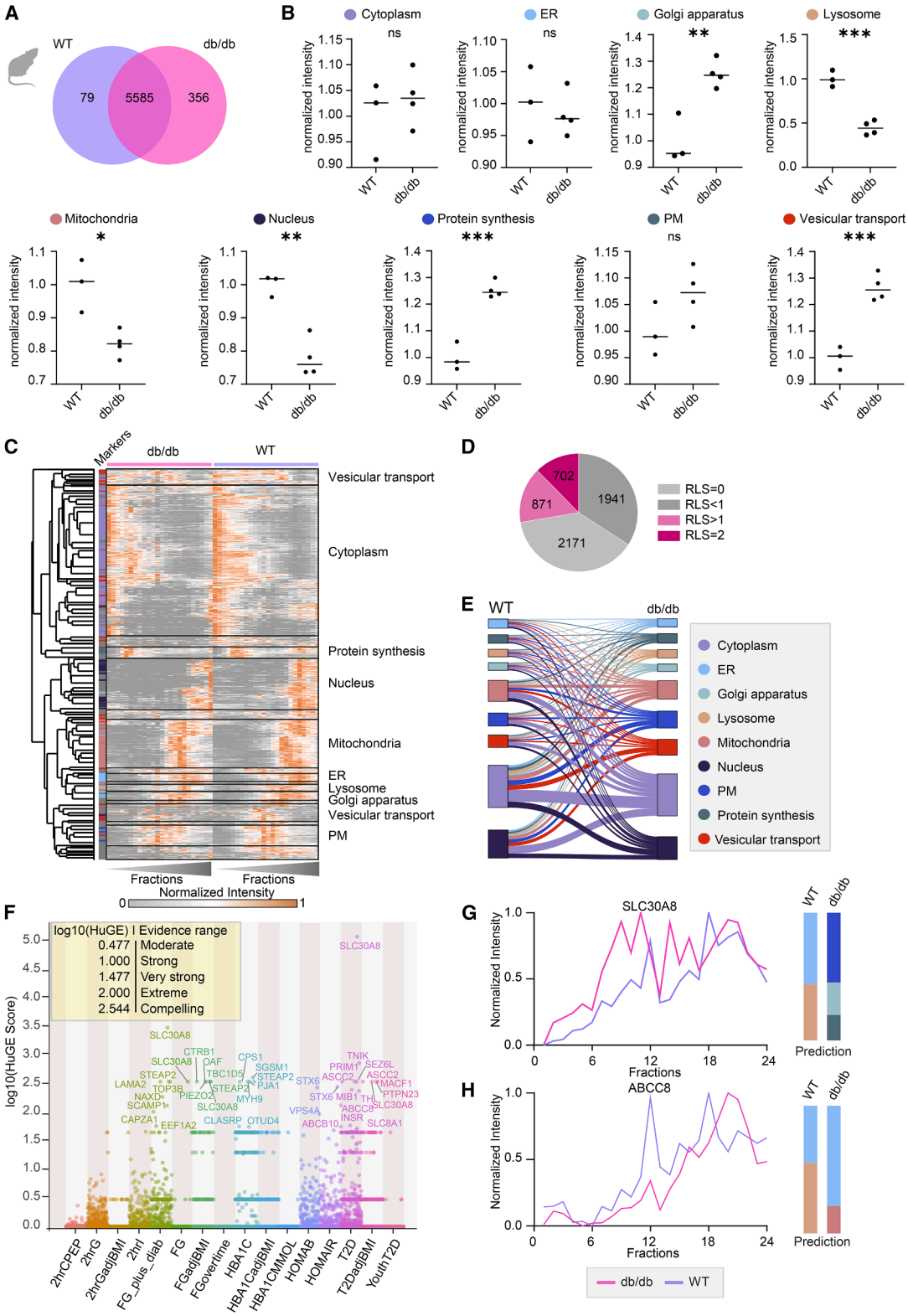

(legend on next page)

ATG5, ATG12, EPG5, VMP1) (Figures S3F–S3H), suggesting active autophagosome formation and possibly increased autophagic activity, potentially due to longer intervals between isolation and fractionation.

Overall, despite the difference in cell composition and maturation state of NICCs compared to human and murine islets, human islets and pig NICCs had greater architectural similarity in localization, consistent with their closer evolutionary relationship.[53] In contrast, mouse islets displayed the most pronounced divergences, particularly affecting pathways critical for β-cell function and insulin secretion. These included components of vesicular trafficking, as well as key regulatory signaling pathways such as cAMP (GNA11), calcium signaling, and cGMP synthesis (GUCY1A1) (Figures S3I–S3K), indicating species-specific differences in the organization of key functional processes.

An organelle map of T2D mice

To investigate alterations in pancreatic islet cellular organization associated with T2D, we used the db/db mouse model, which carries a nonfunctional leptin receptor and consequently develops obesity-induced insulin resistance, islet dysfunction, and hyperglycemia.[54] T2D progression has been well characterized in this model over time: it begins with compensatory hyperinsulinemia driven by β-cell hyperplasia, followed by β-cell failure and overt hyperglycemia.[55,56] Based on detailed phenotyping data (see 8-week phenotyping of JAX stock[57,58]), we selected 8-week-old db/db mice for our analysis. At this age, db/db mice are already obese, have elevated serum lipids (including cholesterol and triglycerides), impaired glucose tolerance, systemic insulin resistance, hyperinsulinemia, and hyperleptinemia. β cells are hypertrophic and under functional stress yet remain largely viable.[59] Consistent with this established phenotype, the mice exhibited elevated blood glucose levels (Figure S4A), in line with a diabetic state at this stage of disease progression. We therefore selected this stage that represents the transitional phase from β-cell compensation to dysfunction to capture cellular changes occurring before widespread β-cell apoptosis to detect early subcellular reorganization. To assess the influence of changes in cell-type abundance on our subcellular map, we quantified cell type markers[46] at the proteome level (Figures S4B–S4D), which revealed a minor decline in β- and δ-cell markers but no evidence of major restructuring of islet cell composition at this time point.

Using PCP on islets isolated from db/db mice, we identified 5,585 proteins shared with our previously generated organelle map from WT islets (Figure 2A). Experimental quality parameters, including the number of proteins detected per fraction, organelle marker profiles, protein distributions across organelles, and the accuracy of localization assignments, were consistent across diabetic and control samples (Figures S4E–S4J). To assess quantitative changes in organelle abundance, we applied the same approach used previously for comparing organelle abundance across species and summed the intensities of organelle marker proteins (Figure 2B). In db/db islets, we observed an increase in abundance of the protein synthesis machinery, Golgi apparatus, and vesicular trafficking pathways, while protein content from mitochondrial, lysosomal, and nuclear compartments was reduced. These shifts are consistent with prior reports showing upregulation of secretory machinery in response to increased insulin demand,[61] as well as mitochondrial loss under chronic glucolipotoxicity.[21]

Despite broadly conserved organelle organization and similar gradient separation behavior between WT and T2D islets (Figure 2C), PCP analysis revealed widespread protein relocalization. To quantify these changes, we used the Relocalization Score (RLS) calculated by C-COMPASS, which measures the degree of compartmental redistribution between conditions. An RLS of zero reflects identical localization, while a score of two indicates complete relocalization. Among all proteins analyzed, 1,573 (∼27%) had an RLS >1, indicating that a substantial fraction of the proteome underwent subcellular redistribution in T2D (Figures 2D and 2E). To validate our approach, we examined pathways known to be affected in T2D or under glucolipotoxicity conditions.[62,63] Proteins associated with stress granules (e.g., SMG, ELAVL4, CNOT2, ATXN2, DDX6), were enriched among re-localized proteins and showed increased profile overlap, suggesting enhanced stress granule formation in diabetic islets (Figures S4K–S4L). In addition, several stress-activated kinases linked to apoptosis, inflammation, and cytoskeletal remodeling, including STK24 and MAP3K7, showed altered localization (Figures S4M and S4N), indicative of signaling changes, as kinase activity is closely tied to subcellular localization.[64–66]

Finally, we integrated our dataset with human genetic data from the HuGeAMP Type 2 Diabetes Knowledge Portal (T2DKP),[60] which aggregates results from over 350 genetic studies on glycemic traits. Among the proteins showing relocalization in db/db islets, we identified 420 proteins with moderate genetic associations (HuGE score $\geq$3) and 329 proteins with strong or very strong associations (HuGE score $\geq$10) to T2D and β-cell dysfunction (Figure 2F; Table S5 for genetic traits explanation). Notably, among the relocalized proteins with high HuGE scores were established regulators of insulin secretion and known therapeutic targets, including the insulin granule-localized zinc transporter SLC30A8 and the KATP channel subunit ABCC8 (Figures 2G and 2H). ABCC8 is a known maturity-onset diabetes of the young (MODY) gene and a clinically validated target of sulfonylureas, which enhances insulin secretion by closing the KATP channel. Overall, protein dynamics and genetic associations point to several candidates as potential drivers of islet dysfunction.

Figure 2. Protein relocalization in T2D model mouse islets

(A) Venn diagram of proteins identified in db/db and WT islets organelle map.

(B) Organelle abundance in WT vs. db/db based on summed marker protein intensities (n = 3 WT, n = 4 db/db; each replicate pooled from five mice, two-sided student's t test, $^{*}p < 0.05$, $^{**}p < 0.01$, $^{***}p < 0.001$, individual data points represent biological replicates. Bars indicate the median, and error bars represent ±SD).

(C) Hierarchical clustering of median 0–1 scaled profiles of common proteins in WT and db/db.

(D) Pie chart of relocalization scores (RLS; 0–2).

(E) Sankey diagram of relocalization events (RLS $\geq$1).

(F) Manhattan plot of HuGE scores from T2DKP[60] for relocalized proteins (RLS $\geq$1) across glycemic traits.

(G and H) PCP profiles of SLC30A8 and ABCC8 with C-COMPASS compartment predictions.

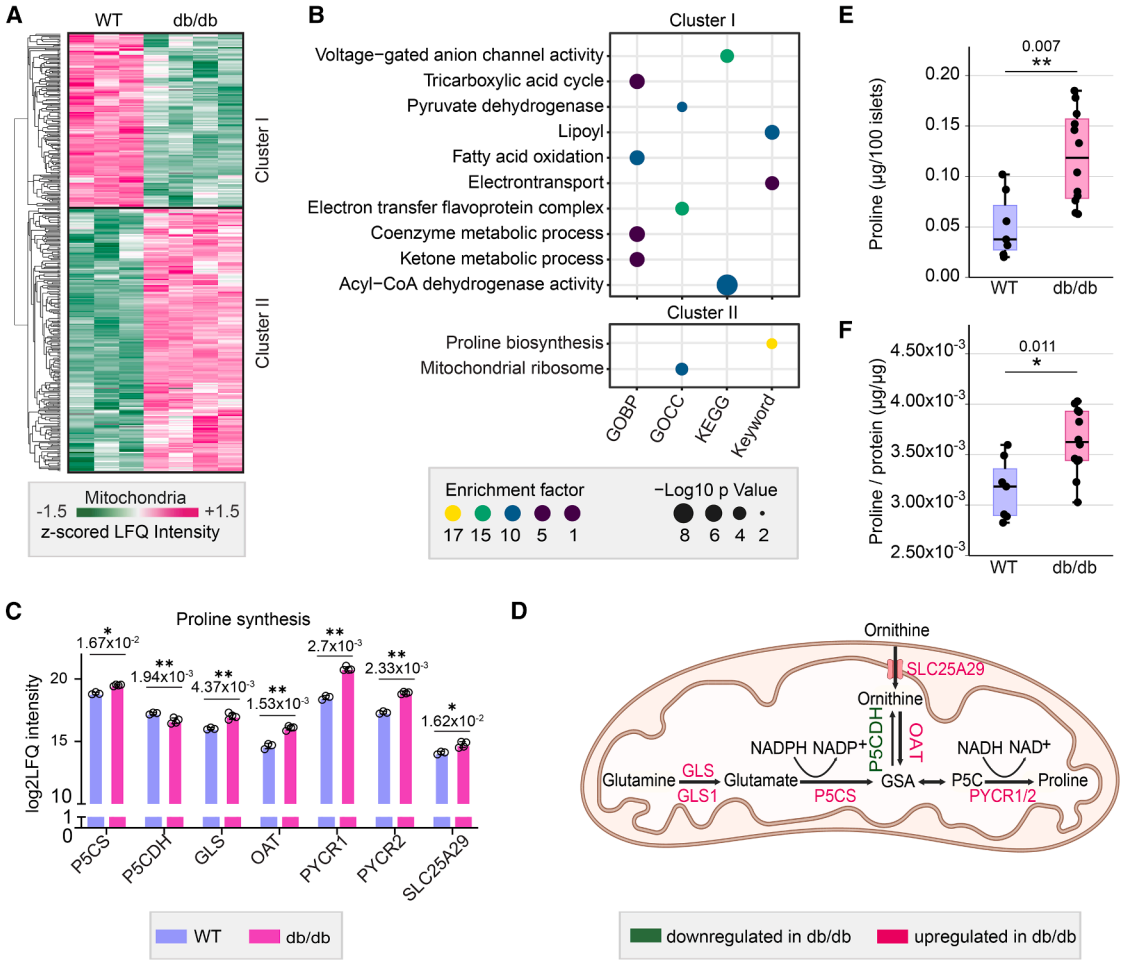

Figure 3. Mitochondrial reprogramming in T2D

(A) Hierarchical clustering of *Z* scored levels of mitochondria-assigned proteins with significantly altered levels in db/db islets (two-sided student's *t* test, FDR <0.05, *n* = 4 db/db, *n* = 3 WT, each replicate pooled from five mice).

(B) GO/KEGG enrichment bubble plot for up- and down-regulated mitochondrial protein clusters (Fisher's exact test, FDR <0.15).

(C) Levels of mitochondrial proline metabolism proteins in WT and db/db islets (two-sided student's *t* test, *FDR <0.05, **FDR <0.01; bars indicate median ±SD).

(D) Schema of mitochondrial proline metabolism with T2D-associated protein level changes indicated.

(E and F) Proline concentrations per 100 islets (µg/100 islets; E) and normalized to protein content (µg/µg protein; F) in WT (*n* = 7) and db/db (*n* = 12) mice. (Boxes show IQR with median; whiskers extend to 1.5× IQR. Mann-Whitney U test; *$p < 0.05$, **$p < 0.01$, ***$p < 0.001$).

Mitochondrial remodeling in T2D

First, given the well-established link between mitochondrial dysfunction and β-cell failure in T2D, and the pronounced decrease in mitochondrial protein abundance observed in our data, we leveraged our organelle proteomics dataset to investigate whether this dysfunction reflects not only a general loss of mitochondrial function and mass, but also remodeling of the mitochondrial proteome and changes of mitochondrial metabolism. To investigate this, we filtered all proteins annotated as mitochondrial in either WT or db/db mice and overlaid these with changes in protein abundance from the total islet proteome. Unsupervised hierarchical clustering of proteins that (i) localized to mitochondria in either condition and (ii) were significantly altered in the total proteome revealed distinct groups of upregulated and downregulated mitochondrial proteins (Figure 3A). Similar results were obtained when proteins were additionally filtered for conserved localization across species (Figures S5A and S5B). Consistent with previous reports of impaired ATP production,[67,68] we observed a downregulation of key metabolic pathways supporting ATP synthesis (Cluster I), including enzymes of the TCA cycle, electron transport chain, and β-oxidation (Figure 3B). Interestingly, despite this overall decline in mitochondrial metabolic activity, we detected a coordinated upregulation of enzymes involved in proline biosynthesis from either glutamine or ornithine in mitochondria (Cluster II) (Figure 3B). Enzymes mediating the conversion of glutamine to proline, such as GLS1 (glutaminase) and P5CS (ALDH18A1, pyrroline-5-carboxylate synthase), were elevated. Similarly, levels of OAT (ornithine aminotransferase) and SLC25A29, a mitochondrial ornithine transporter, increased. Enzymes

catalyzing the final step of proline synthesis, PYCR1 and PYCR2 (pyrroline-5-carboxylate reductase 1 and 2), which convert pyrroline-5-carboxylate (P5C) to proline, also showed elevated levels, while P5CDH (ALDH4A1, pyrroline-5-carboxylate dehydrogenase), responsible for proline degradation, was downregulated (Figure 3C). Together, these changes indicate a metabolic shift toward proline accumulation (Figure 3D). As determined by LC-MS, proline levels were significantly elevated in islets isolated from db/db mice compared with WT controls (Table S6). When expressed per islet number, proline concentrations were 3.15-fold higher in db/db islets than in WT islets (Figure 3E). This increase remained statistically significant after normalization to total protein content to account for potential differences in islet mass (Figure 3F). Proline synthesis has been shown to mitigate mitochondrial oxidative stress by regenerating NAD^+ and supporting redox homeostasis under conditions of electron transport chain dysfunction.[69] While this may represent an adaptive response to redox stress, elevated proline levels may have detrimental effects. Proline serves as a precursor for collagen synthesis, and its accumulation may promote extracellular matrix (ECM) production and islet fibrosis, a pathological feature of T2D.[63] Furthermore, excessive proline has been implicated in pancreatic islet dysfunction via amino acid toxicity, impairing insulin secretion and exacerbating β-cell failure.[70]

To test whether these changes are conserved in humans, we first performed 1D annotation enrichment on the published total tissue proteome comparing healthy and T2D from the Human Islet platform,[71,72] currently the largest resource for proteomic profiling of human islets, including datasets from individuals with T2D (Figure S5C). This method ranks proteins by their fold change and identifies functional categories that shift along this gradient, thereby highlighting pathways that are systematically up- or down-regulated. At the total proteome level, we observed downregulation of TCA cycle components, electron transport chain complexes, and ATP synthesis machinery. In parallel, we applied a complementary workflow in which we first filtered proteins assigned to mitochondria based on our PCP localization approach and then overlaid these with changes reported in the Human Islet platform[71,72] T2D dataset. This revealed an upregulated mitochondrial cluster enriched for proline and arginine biosynthesis pathways, whereas TCA cycle and pyruvate metabolism were consistently downregulated (Figures S5D and S5E). Together, these findings indicate that a loss of mitochondrial energy metabolism and a shift toward altered amino acid metabolism, particularly increased proline synthesis, are conserved features across species.

Altered vesicular trafficking and phosphoinositide metabolism in T2D

Next, to investigate subcellular changes in a systematic unbiased manner and identify the most dysregulated pathways, we performed enrichment analysis on relocalized proteins (Figure 4A). In T2D islets, these proteins were significantly enriched in vesicular transport pathways, including components involved in vesicle fusion, priming, and docking, suggesting widespread restructuring or dysfunction of the insulin secretory machinery. This aligns with the previously reported impairment of glucose-stimulated insulin secretion in T2D with early loss of first-phase secretion as a hallmark.[73] Moreover, previous studies have reported reduced numbers of docked insulin granules, disrupted spatial organization at the plasma membrane, and defective signaling pathways regulating granule docking in βcells from T2D donors.[74,75]

Using PCP-based localization profiling, we characterized molecular alterations underlying these defects. Focusing on proteins assigned to the vesicular trafficking compartment, we modeled compositional changes using whole-islet proteomics, analogous to our mitochondrial analysis. Specifically, we performed unsupervised hierarchical clustering on proteins annotated with vesicular transport localization in either WT or db/db mice and applied an additional filter for those showing significant changes in the total islet proteome (with conserved localization across species, as added criteria shown in Figures S6A and S6B). This analysis revealed upregulation of proteins involved in vesicle formation and cargo selection, including clathrin, COPI, COPII, and AP adapter complexes (Figures 4B and 4C), likely reflecting the increased basal secretion and compensatory response to increased secretory demands in T2D.[76] However, the subcellular localizations of many of those upregulated key vesicular trafficking proteins, including entire protein complexes essential for this process, were altered, questioning their proper functionality in T2D. For instance, proteins critical for insulin granule fusion such as the core SNARE machinery components (e.g., STXBP1, STXBP2) had changed localizations (Figure 4D; Figure S6C). Similarly, proteins required for vesicle priming and docking, including VAMP4,[77] were relocalized (Figure S6D). Additionally, endosomes, particularly recycling endosomes, were enriched among relocalized proteins. These compartments are critical for recycling insulin granule components and membrane receptors such as glucagon-like peptide 1 receptor (GLP1R), gastric inhibitory polypeptide receptor (GIPR), and insulin receptor (INSR), which play important roles in regulating insulin secretion and β-cell function and are major drug targets.[78] We identified widespread reorganization and downregulation within the endosomal recycling machinery, including the small GTPases (RAB8B, RAB10, RAB22A) and EHD-family ATPases (EHD2-4), which mediate membrane remodeling and endosome formation[79] (Figure 4E; Figure S6E). Components of the retromer complex (e.g., SNX1, SNX2, VPS29, VPS35), responsible for retrieving cargo from endosomes to the Golgi apparatus or plasma membrane,[80] also showed altered localization with a shift to cytosolic fractions, indicating complex disassembly (Figures S6F–S6G).

In parallel, pathway enrichment analysis (Figure 4A) revealed alterations in phosphoinositide (PI) signaling, a pathway closely linked with vesicular trafficking. PI-metabolizing enzymes generate spatial lipid gradients that define membrane identity, recruit effector proteins, and thereby regulate granule formation, maturation, trafficking, and fusion.[81,82] Accordingly, disruptions in PI metabolism can lead to the mislocalization of key trafficking components and functional impairment of the secretory pathway. Numerous PI metabolizing enzymes and PI-binding proteins showed altered localization in T2D, including PI4KA, PI4K2A, PIK3C3, PIK3C2A, PIP4P1, PTEN, PIK3R1, PI4K2B, PIKFYVE, PLEKHA1, and PIP5K1C. For

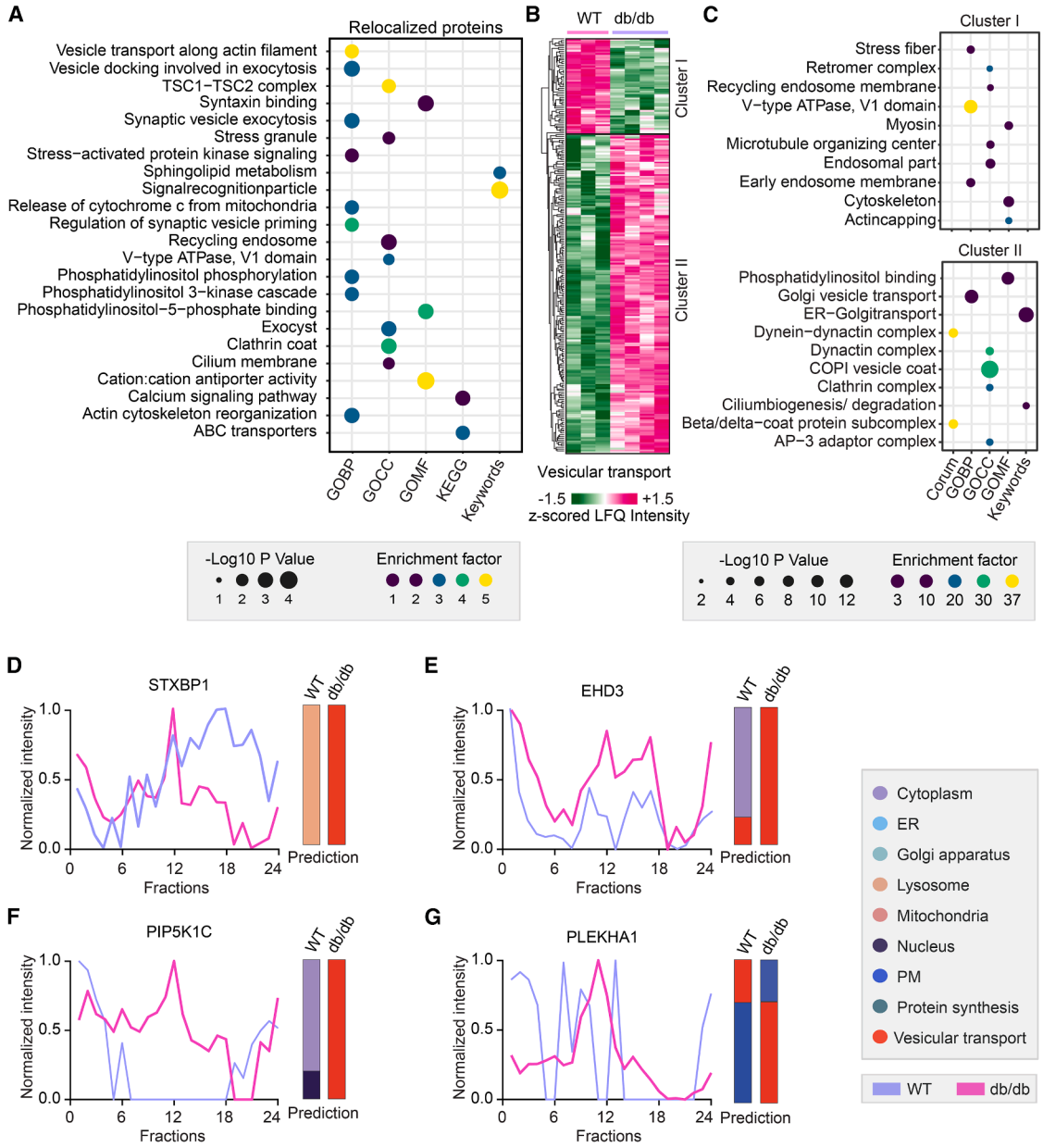

Figure 4. Altered vesicular trafficking and phosphoinositide metabolism in T2D

(A) GO/KEGG enrichment bubble plot of relocalized proteins (one-sided Fisher's exact test, FDR <0.15).

(B) Hierarchical clustering of *Z* scored levels of vesicular transport proteins significantly altered in db/db islets (two-sided student's *t* test, FDR <0.05, $n = 4$ db/db, $n = 3$ WT).

(C) GO/KEGG enrichment bubble plot for up- and down-regulated clusters.

(D–G) PCP profiles of indicated proteins with C-COMPASS compartment predictions represented as bars (median profiles, $n = 4$ db/db, $n = 3$ WT, each replicate represents pooled islets from five mice).

example, PIP5K1C and PTEN, which regulate $PI(4,5)P_2$ and $PI(3,4,5)P_3$ at the plasma membrane,[83,84] respectively, showed increased recruitment to vesicular and plasma membrane fractions (Figure 4F; Figure S6H). This was accompanied by enhanced membrane association of $PI(4,5)P_2$-binding proteins such as PLEKHA1 (Figure 4G). Many of these proteins are associated with glycemic traits in the T2DKP,[60] highlighting their relevance for insulin secretion and β-cell function (Figure S6I).

To test for the conservation of this regulation in the human islet proteome in T2D, we next analyzed the levels of vesicular trafficking proteins in the human total islet proteome comparing T2D donors and healthy donors from the Human Islet platform,[71,72] 1D annotation enrichment and pathway analysis of

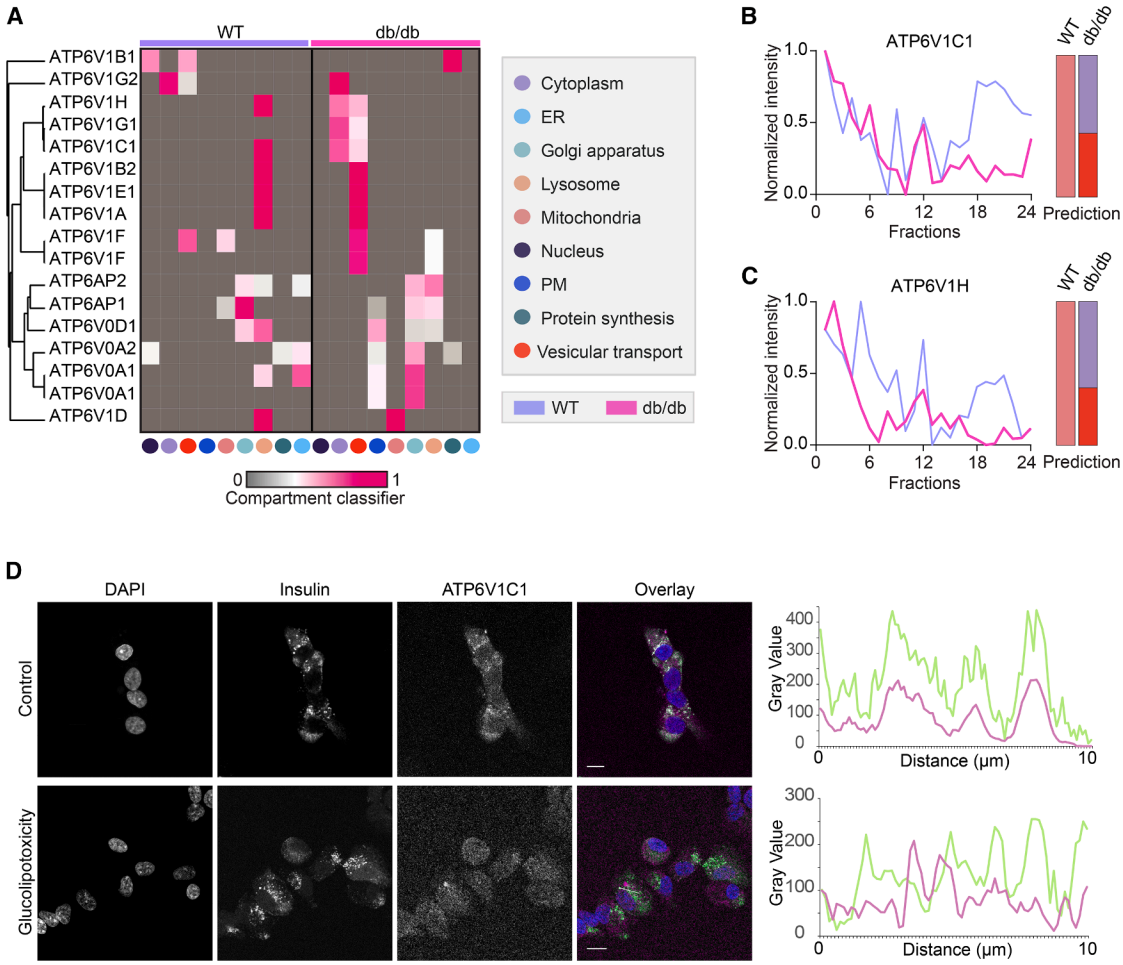

Figure 5. Dissociation of the V-type ATPase complex in T2D

(A) Hierarchical clustering of C-COMPASS compartment classifiers for all detected V-type ATPase subunits in WT and db/db.

(B and C) PCP profiles of indicated subunits with C-COMPASS predictions (median, $n = 4$ db/db, $n = 3$ WT).

(D) Immunofluorescence of ATP6V1C in EndoC-βH5 cells under normal and glucolipotoxic conditions (DAPI, blue; insulin, green; ATP6V1C, magenta; scale bars, 10 μm; $n = 3$ experiments) with fluorescence intensity line plots across the indicated lines.

up- and down-regulated vesicular trafficking proteins revealed broad downregulation of pathways involved in exocytosis and vesicular trafficking (Figures S6J–S6L). Downregulated categories included regulation of synaptic vesicle exocytosis and endocytosis, components of the endomembrane system, SNARE complex proteins, syntaxins, clathrin-mediated processes, and factors required for vesicle docking and priming. Taken together, these findings indicate a profound reorganization of the vesicular trafficking machinery in T2D islets in mouse and human, indicating remodeling of the secretory apparatus underlying defective insulin secretion in the disease.

Impairment of the insulin granule acidification machinery

An additional key finding from our enrichment analysis was the altered localization of proteins comprising the V1 subunit of the V-type ATPase complex in mice (Figure 4A) and humans (Figures S6J–S6L). This proton pump is essential for lysosomal and insulin granule acidification. This acidification is crucial for insulin processing and granule maturation, as the enzymes involved require an acidic environment to function.[85,86] The functional V-type ATPase consists of a membrane-anchored V0 subunit and an attached cytosolic catalytic V1 subunit.[87] In diabetic mice, we observed a shift of most V1 subunits from membrane-bound to cytosolic and vesicular fractions of lower density, while in the healthy state, the V1 subunits floated at fractions of high density where lysosomes and insulin granules sediment (Figures 5A–5C). This V-type ATPase disassembly could be recapitulated in EndoC-βH5, a human pancreatic islet model. Glucolipotoxicity treatment for 48 h was sufficient to induce dissociation of the V-type ATPase complex, as confirmed by immunofluorescence for ATP6V1C. Compared to untreated cells, a more diffuse cytosolic staining and less colocalization with insulin was observed (Figure 5D). This dissociation is a conserved regulatory mechanism that typically suppresses ATPase activity,[88] thereby suggesting a decrease in V-type

CellPress
OPEN ACCESS

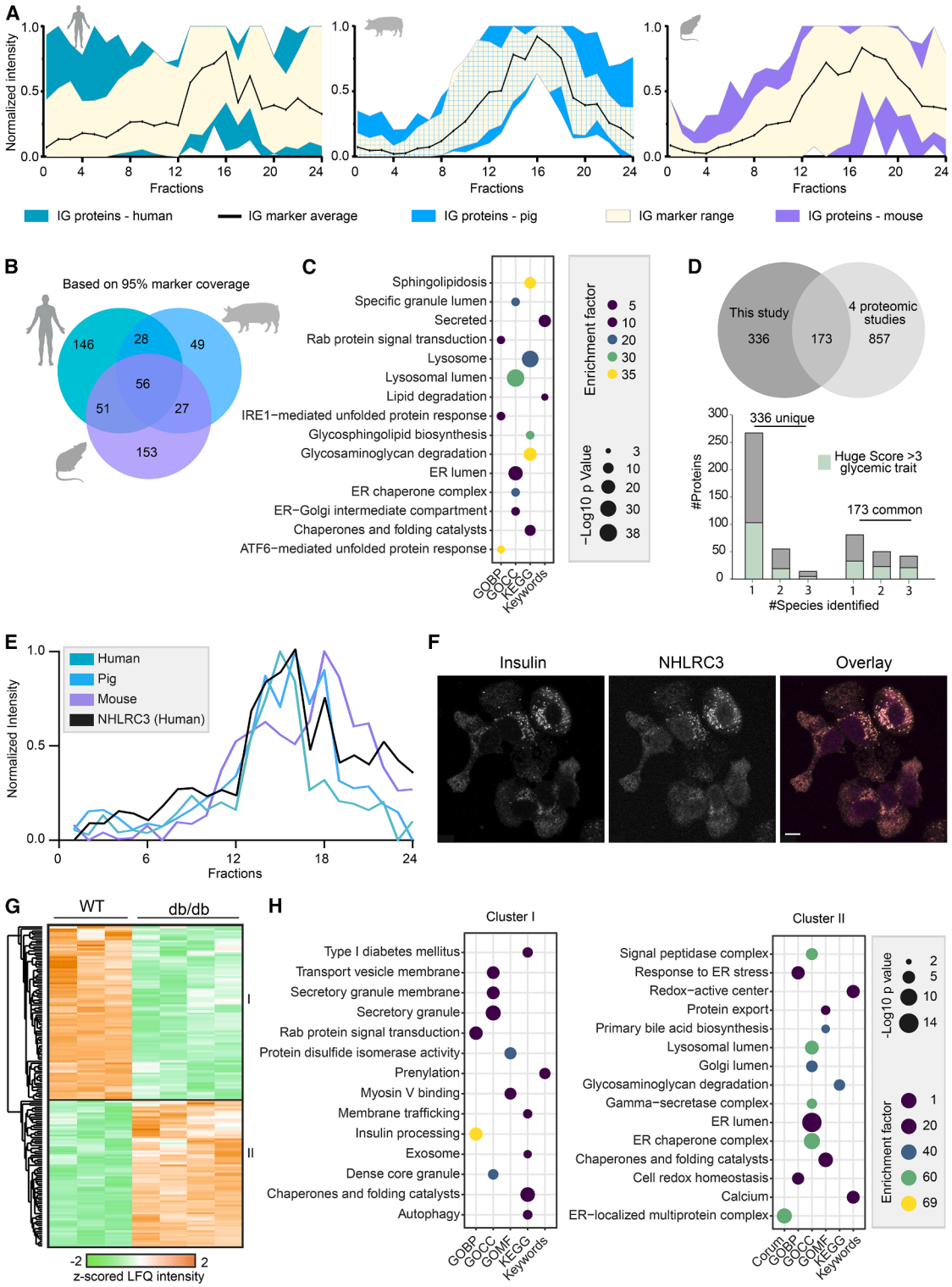

Figure 6. Mapping the insulin granule proteome

(A) Median and range of insulin granule marker profiles and granule-assigned proteins per species.

(B) Venn diagram of insulin granule proteins across species.

(C) GO/KEGG enrichment of granule proteins conserved in ≥2 species (one-sided Fisher's exact test, FDR <0.15).

(legend continued on next page)

ATPase activity. Concurrently, our proteomic analysis revealed a downregulation of the complex, implying that disassembly could be followed by protein degradation (Figures S6M–S6N). A significant downregulation of several V-type ATPase V1 subunits was also detected in the proteome of human T2D islets from the Human Islet platform[71,72] (Figure S6O). The combined disassembly and subsequent reduction in the protein levels of the V1 subunit suggest a compromised V-type ATPase function. This likely leads to diminished acidification of insulin granules, thereby impairing insulin processing which might contribute to pancreatic islet dysfunction in T2D.

Insulin granule composition and its T2D alterations

Several studies have aimed to define the insulin granule proteome, primarily using β-cell lines such as Min6 and INS-1 cells.[89–91] However, to our knowledge, no *in vivo* proteomic study has characterized the insulin granule proteome from isolated pancreatic islets. Given the limited number of well-defined markers that localize exclusively to insulin granules, directly applying the C-COMPASS pipeline for this purpose was not feasible. Therefore, we developed an alternative strategy to identify insulin granule proteins within our PCP dataset. Specifically, we selected protein profiles with high similarity to canonical insulin granule markers, calculating Euclidean distances between each protein and a median profile derived from 19 well-established granule marker proteins (Figure S7A). To ensure robustness, we selected proteins within the 95th percentile of marker similarity for each species (Figure 6A). This approach yielded 162 proteins shared by at least two species, and 56 proteins common to all three species (Figure 6B; Figure S7B). Enrichment analysis of the cross-species hits revealed functional categories characteristic of the insulin granule proteome, including secreted proteins, granule lumen components, ER-associated folding machinery, lysosomal proteins (frequently co-localized with granules[90]), and Rab GTPases essential for granule trafficking (Figure 6C).

To identify novel insulin granule components, we compared our candidate list with previously published state-of-the-art proteomes.[89–92] Out of 509 candidates identified in any of the species, 173 overlapped with known insulin granule proteins, while 336 were unique to our study (Figure 6D). Among these novel candidates, 69 were conserved across at least two species and 109 showed genetic associations with glycemic traits (Figure S7C). Immunofluorescence microscopy in EndoC-βH5 cells confirmed the co-localization of several candidate proteins such as P4HB and PGRMC1 with insulin granules (Figure S7D). Among these, we identified NHLRC3 as a previously uncharacterized granule-associated protein that is conserved across species. NHLRC3 is of unknown function, with predicted secreted and intracellular isoforms, and exhibits moderate genetic associations with HOMA-B[60] (homeostatic model assessment of β-cell function), a trait that reflects β-cell function and insulin sensitivity based on fasting glucose and insulin levels (Figures 6E and 6F; Figure S7C). These findings suggest that NHLRC3 may represent a yet unknown component of the insulin granule proteome.

Finally, we investigated changes in insulin granule composition under T2D conditions. Proteomic analysis of total islet lysates from db/db mice revealed a downregulation of granule lumen proteins, including INS1, INS2, SCG2, SCG3, and CPE, as well as reduced levels of Rab proteins involved in granule trafficking (Figures 6G and 6H). In contrast, proteins associated with ER-mediated protein folding and quality control were upregulated, likely to reflect a compensatory response to increased secretory stress in β cells. In human islets, assessments of the insulin granule proteome in T2D from the Human Islet platform[71,72] revealed fewer significant alterations. Insulin abundance itself was unchanged, and only a subset of granule-associated proteins showed differential expression, including reduced levels of insulin-processing enzymes such as PCSK1 and the granule protein CHGA (Figure S7E). Overall, we show that our atlas can be used to identify previously unrecognized granule components conserved across species and assess insulin granule remodeling during islet dysfunction in T2D.

DISCUSSION

By integrating PCP with neural network-based compartment classification, we generated an organelle atlas of pancreatic islets across humans, mice, and pig NICCs. The atlas resolves nine major cellular compartments and provides information about localization for more than 8,000 proteins. It also provides the first *in vivo* proteomic map of insulin secretory granules, offering a resource for dissecting granule biology and its perturbation in T2D. The resulting organelle maps reflect mixed islet cell-type signatures, with a strong β-cell contribution in mice and humans, consistent with their high endocrine abundance, and a comparatively lower β-cell influence in pig NICCs. Although individual proteins integrate contributions from different cell types to their localization profiles, current methods do not yet allow deconvolution of these effects. To demonstrate the utility of the atlas for hypothesis generation, we confirmed the presence of previously unrecognized insulin granule proteins and validated the disassembly of the V-type ATPase in T2D-mirroring conditions using EndoC-βH5 cells, a human β-cell model. These findings exemplify how the atlas can guide cell type-specific downstream experiments.

Focusing on molecular remodeling in pancreatic islets during T2D, in the db/db mouse model, we observed substantial changes of organelle abundance and relocalization of approximately 30% of the entire proteome. Specifically, we saw a compensatory upregulation of vesicular trafficking, the Golgi apparatus, and the protein synthesis machinery, likely triggered

(D) Overlap of insulin granule proteome of this study with four published granule proteomes (Li et al.,[92] Brunner et al; ,[90] Neukam et al;[89] and Norris et al;[91]) and genetic associations (HuGE ≥3 in T2DKP[60]).
(E) NHLRC3 protein profile across species with insulin granule average profiles from the three species.
(F) Immunofluorescence of NHLRC3 in EndoC-BH5 (insulin, yellow; NHLRC3, magenta; scale bars, 10 μm; n = 2–3).
(G) Hierarchical clustering of Z scored levels of significantly changed granule proteins in db/db (two-sided student's t test, FDR <0.05).
(H) GO/KEGG enrichment for up- (cluster I) and down-regulated (cluster II) granule proteins in db/db.

by the activation of the unfolded protein response (UPR)-mediated stress response.[93] However, many of the upregulated factors in vesicular transport, including crucial insulin granule docking and fusion complexes, were mislocalized. This mislocalization suggests that merely increasing the abundance of these components may not rectify the underlying dysfunction and might explain the persistent defects in the secretory function in T2D.[74] We identified previously unknown processes underlying pancreatic islet failure in T2D including (1) changes in mitochondrial amino acid metabolism potentially promoting proline accumulation, (2) the reorganization of the vesicular trafficking machinery, (3) the spatial reorganization of the PI signaling cascade, and (4) the dissociation and downregulation of V-type ATPase V1 subunit.

Upregulation of mitochondrial proline synthesis machinery

We identified mitochondrial reprogramming in pancreatic islets as a potential contributor to T2D progression. While core mitochondrial functions, particularly those essential for ATP synthesis, insulin secretion, and glucose responsiveness, were impaired, there was a concurrent upregulation of the mitochondrial proline synthesis pathway. This shift, mediated by P5CS and PYCR enzymes, promotes NAD^+ regeneration and supports redox homeostasis under conditions of respiratory impairment and oxidative stress, both of which are hallmarks of T2D β cells.[94] These findings suggest a compensatory response aimed at counteracting redox imbalance. However, chronic proline accumulation has been associated with β-cell dysfunction and impaired insulin secretion.[70] In addition, elevated proline levels stimulate collagen production, contributing to ECM buildup.[69] We hypothesize that this metabolic shift may exacerbate islet fibrosis, a hallmark of T2D,[95] through increased proline availability in the tissue, potentially fueling ECM deposition by pancreatic stellate cells and fibroblasts. Fibrosis disrupts the islet microenvironment, impairing β-cell plasticity, motility, and functional adaptability, thereby further compromising insulin secretion and promoting disease progression.[96]

Vesicular trafficking and PI metabolism

An unresolved question emerging from our data is the causal relationship between vesicular trafficking reorganization and disrupted PI signaling. Specifically, it remains unclear whether the observed changes in vesicular trafficking are a consequence of altered PI signaling, or if they actively drive the PI signaling disruptions. Regardless of directionality, it is evident that these alterations have profound implications for insulin secretion. The relocalization of PI-synthesizing and turnover enzymes likely disrupts PI gradients, which are essential for maintaining organelle identity and regulating vesicle dynamics.[97] For example, mislocalization of PIP5K1C and PTEN could impair vesicle exocytosis at the plasma membrane. PTEN dephosphorylates $PI(3,4,5)P_3$, reducing its levels,[98] while PIP5K1C phosphorylates PI4P to generate $PI(4,5)P_2$.[99] Disruption of this balance alters the recruitment of PI-binding proteins, including PH- and C2-domain-containing effectors, which are critical for exocytosis and cytoskeletal regulation.[100] Such imbalances may lead to uncoordinated granule docking, premature exocytosis, and impaired granule recycling. Moreover, elevated $PI(4,5)P_2$ levels have been shown to activate KATP channels,[101] resulting in membrane hyperpolarization and a subsequent reduction in insulin secretion. Together, these findings highlight a severe dysregulation of pancreatic islet function, where disrupted PI signaling and vesicle mislocalization together compromise the physiological insulin response.

V-type ATPase disassembly

Our subcellular atlas revealed a previously unknown mechanism underlying pancreatic islet dysfunction in T2D: the dissociation of the V1 subunit of V-type ATPase. This dissociation is a known conserved mechanism to regulate the complex's activity. It is tightly regulated by signaling pathways such as PKA and AMPK, which modulate its function to conserve energy by reducing ATP hydrolysis and proton pumping during periods of low metabolic demand.[102,103] However, in T2D, the ongoing dissociation, along with the downregulation of the V1 subunit, suggests a maladaptive response, leading to the cellular failure to maintain proper V-type ATPase activity. Strikingly, a significant downregulation of V1 ATPase subunits was also detectable in the human pancreatic islet proteome derived from the Human Islet platform,[71,72] indicating that this mechanism also underlies β-cell dysfunction in human T2D. V-type ATPase acidifies insulin granules necessary to activate prohormone convertases that process proinsulin into insulin and C-peptide.[85,86] Impaired V-type ATPase function leads to incomplete proinsulin processing, accumulation of improperly processed insulin, and the production of defective granules that cannot efficiently release insulin.[104] Additionally, V-type ATPase is functioning in lysosomal acidification and therefore important for lysosomal activity. Lysosomes degrade and recycle misfolded or aggregated insulin, thereby impacting β-cell proteostasis.[105] Over time, these defects in insulin processing, secretion, and proteostasis will result in chronic β-cell stress, reduced insulin secretion capacity, and ultimately β-cell failure. This raises the possibility that V-type ATPase dysfunction could be a key contributor to β-cell failure, disease progression and a potential target for therapeutic intervention to preserve pancreatic islet function.

Limitations of the study

A primary limitation of our study is the resolution of subcellular compartments. Due to overlapping sedimentation profiles, certain organelles, such as peroxisomes, could not be distinctly resolved, and endosomes and transport vesicles were grouped under a broad "vesicular trafficking" category. Furthermore, our approach does not differentiate between readily releasable and reserve insulin granule pools, limiting the ability to capture the full spectrum of insulin granule dynamics. Another major limitation is the large material requirement for organelle proteomics, which constrains throughput. As a result, we could only include a small number of human and pig samples and cannot systematically explore sex differences or include more human donors. Consequently, our data do not sufficiently capture human variability. Moreover, the human, pig, and mouse samples analyzed represent different developmental stages, older humans, neonatal *in vivo*-matured pigs, and young mice. Age- and maturation-related effects may therefore contribute to the observed

differences in organelle organization. Additionally, organelle mapping was performed on whole islets rather than sorted cell populations, due to limited material availability. The resulting profiles may be dominated by β cells in mouse islets, where βcells comprise 70%–80% of islet cells, but they also include signals from other endocrine cell types. This limitation is more pronounced in human islets, where β-cell representation is lower (∼50%–60%)[5] and especially in pig NICCs where the β cells make 30% of all cells in the tissue. Unfortunately, it is currently not possible to deconvolute the contribution of single cell types to the localization profiles. Importantly, differences in cell type composition between species, or between healthy and T2D islets (e.g., β-cell loss and α/δ-cell expansion), could also influence the observed localization profiles, confounding direct cross-species and disease-state comparisons. Furthermore, species-specific differences in islet isolation and handling protocols, as well as differences in islet architecture, which likely support more heterotypic cell-cell interactions and could affect subcellular organization and signaling networks may influence proteomic outcomes. Finally, due to the limited availability of fresh human T2D islets in large quantities, we relied on a murine model to examine disease-associated remodeling. While we could confirm key findings in human EndoC-βH5 cells in glucolipotoxicity, the species-specific differences in β-cell physiology mapped in this and other studies, underscore the need for future studies leveraging human islets to extend these findings.

RESOURCE AVAILABILITY

Lead contact

Requests for further information and resources should be directed to and will be fulfilled by the lead contact, Natalie Krahmer (natalie.krahmer@helmholtz-munich.de).

Materials availability

This study did not generate new unique reagents.

Data and code availability

Proteomics data generated in this study are available on the PRIDE repository (ProteomeXchange)[106] under the accession number PXD064528. Metabolomics data including peak area tables, calibration information, and annotated chromatograms are provided in Table S6. No customized code has been developed for this study. Original data for each figure is provided in the resource files. All other data will be shared upon request.

ACKNOWLEDGMENTS

We thank all members of the Krahmer laboratory for discussions. We thank Sara Ribicic for technical assistance. We thank the Helmholtz Munich Proteomics Core Facility and Juliane Merl-Pham for their support. We thank all donors and their families. These studies were supported by DFG Emmy Noether (KR5166/1 to N.K.), the European Foundation for the Study of Diabetes (Future Leader Award NNF20SA0066171 to N.K). P.C. was supported by the International Helmholtz Research School for Diabetes, funded by the Helmholtz Association – Initiative and Networking Fund. T.D.M received funding from European Research Council ERC-CoG trusted no. 101044445 and by the German Research Foundation (grant nos. DFG TRR296, TRR152, SFB1123, and GRK 2816/1).

AUTHOR CONTRIBUTIONS

N.K. and Ö.S.C. conceived the project and designed experiments. Ö.S.C. performed organelle fractionations and microscopy. Ö.S.C. and D.T.H. performed proteomic analyses. Ö.S.C., D.T.H, and N.K. analyzed data. A.B.-P., P.C., S.B., M.T.-M., S.C., J.V.F., J.J., O.C., P.K., D.B., V.G, C.D., H.D.d.l.H., and M.B. maintained mice and isolated murine islets. E.W., E.,K. and M.S. provided and characterized neonatal pig islets. A.C.-S. provided discussion, T.D.M. and H.L. provided resources, discussions, manuscript revision, and data interpretation. N.K., Ö.S.C., and D.T.H. wrote the manuscript.

DECLARATION OF INTERESTS

H.L. reports financial support was provided by European Union. H.L. reports financial support was provided by Federal Ministry of Education and Research Bonn Office. T.D.M. receives research funding by Novo Nordisk. The other authors declare no competing interests.

STAR★METHODS

Detailed methods are provided in the online version of this paper and include the following:

- KEY RESOURCES TABLE
- EXPERIMENTAL MODELS AND STUDY PARTICIPANT DETAILS
  - Mice
  - Human pancreatic islets
  - Ethics statement
  - Pigs
  - EndoC cells
- METHOD DETAILS
  - Pancreatic islet isolations
  - Cell culture
  - Immunofluorescence
  - Organelle separation
  - Proteomics
  - Metabolomics
- QUANTIFICATION AND STATISTICAL ANALYSIS
  - Statistics analysis
  - Proteome raw data processing
  - Proteome analysis
  - C-COMPASS analysis
  - Organelle modeling
  - Organelle quantification
  - Insulin granule protein identification
  - Metabolomic data analysis

SUPPLEMENTAL INFORMATION

Supplemental information can be found online at https://doi.org/10.1016/j.celrep.2026.117751.

Received: September 9, 2025
Revised: June 12, 2026
Accepted: July 9, 2026

REFERENCES

1. Hauge-Evans, A.C., King, A.J., Carmignac, D., Richardson, C.C., Robinson, I.C.A.F., Low, M.J., Christie, M.R., Persaud, S.J., and Jones, P.M. (2009). Somatostatin secreted by islet delta-cells fulfills multiple roles as a paracrine regulator of islet function. Diabetes *58*, 403–411. https://doi.org/10.2337/db08-0792.
2. Huising, M.O. (2020). Paracrine regulation of insulin secretion. Diabetologia *63*, 2057–2063. https://doi.org/10.1007/s00125-020-05213-5.
3. Jeon, J., Correa-Medina, M., Ricordi, C., Edlund, H., and Diez, J.A. (2009). Endocrine Cell Clustering During Human Pancreas Development. J. Histochem. Cytochem. *57*, 811–824. https://doi.org/10.1369/jhc.2009.953307.

4. Tritschler, S., Thomas, M., Böttcher, A., Ludwig, B., Schmid, J., Schubert, U., Kemter, E., Wolf, E., Lickert, H., and Theis, F.J. (2022). A transcriptional cross species map of pancreatic islet cells. Mol. Metab. *66*, 101595. https://doi.org/10.1016/j.molmet.2022.101595.

5. Cabrera, O., Berman, D.M., Kenyon, N.S., Ricordi, C., Berggren, P.O., and Caicedo, A. (2006). The unique cytoarchitecture of human pancreatic islets has implications for islet cell function. Proc. Natl. Acad. Sci. USA *103*, 2334–2339. https://doi.org/10.1073/pnas.0510790103.

6. Brereton, M.F., Iberl, M., Shimomura, K., Zhang, Q., Adriaenssens, A.E., Proks, P., Spiliotis, I.I., Dace, W., Mattis, K.K., Ramracheya, R., et al. (2014). Reversible changes in pancreatic islet structure and function produced by elevated blood glucose. Nat. Commun. *5*, 4639. https://doi.org/10.1038/ncomms5639.

7. Steiner, D.J., Kim, A., Miller, K., and Hara, M. (2010). Pancreatic islet plasticity: interspecies comparison of islet architecture and composition. Islets *2*, 135–145. https://doi.org/10.4161/isl.2.3.11815.

8. MacDonald, M.J., Longacre, M.J., Stoker, S.W., Kendrick, M., Thonpho, A., Brown, L.J., Hasan, N.M., Jitrapakdee, S., Fukao, T., Hanson, M.S., et al. (2011). Differences between human and rodent pancreatic islets: low pyruvate carboxylase, atp citrate lyase, and pyruvate carboxylation and high glucose-stimulated acetoacetate in human pancreatic islets. J. Biol. Chem. *286*, 18383–18396. https://doi.org/10.1074/jbc.M111.241182.

9. Cook, D.L., and Hales, N. (1984). Intracellular ATP directly blocks K+ channels in pancreatic B-cells. Nature *311*, 271–273. https://doi.org/10.1038/311271a0.

10. Komatsu, M., Takei, M., Ishii, H., and Sato, Y. (2013). Glucose-stimulated insulin secretion: A newer perspective. J. Diabetes Investig. *4*, 511–516. https://doi.org/10.1111/jdi.12094.

11. Dean, P.M. (1973). Ultrastructural morphometry of the pancreatic -cell. Diabetologia *9*, 115–119. https://doi.org/10.1007/BF01230690.

12. Campelo, F., Tian, M., and von Blume, J. (2023). Rediscovering the intricacies of secretory granule biogenesis. Curr. Opin. Cell Biol. *85*, 102231. https://doi.org/10.1016/j.ceb.2023.102231.

13. Fan, J., Wang, Y., Liu, L., Zhang, H., Zhang, F., Shi, L., Yu, M., Gao, F., and Xu, Z. (2017). cTAGE5 deletion in pancreatic beta cells impairs proinsulin trafficking and insulin biogenesis in mice. J. Cell Biol. *216*, 4153–4164. https://doi.org/10.1083/jcb.201705027.

14. Weir, G.C., and Bonner-Weir, S. (2004). Five stages of evolving beta-cell dysfunction during progression to diabetes. Diabetes *53*, S16–S21. https://doi.org/10.2337/diabetes.53.suppl_3.s16.

15. Müller, A., Schmidt, D., Xu, C.S., Pang, S., D'Costa, J.V., Kretschmar, S., Münster, C., Kurth, T., Jug, F., Weigert, M., et al. (2021). 3D FIB-SEM reconstruction of microtubule-organelle interaction in whole primary mouse beta cells. J. Cell Biol. *220*, e202010039. https://doi.org/10.1083/jcb.202010039.

16. Stützer, I., Esterházy, D., and Stoffel, M. (2012). The pancreatic beta cell surface proteome. Diabetologia *55*, 1877–1889. https://doi.org/10.1007/s00125-012-2531-3.

17. Bartolome, A., Guillen, C., and Benito, M. (2012). Autophagy plays a protective role in endoplasmic reticulum stress-mediated pancreatic beta cell death. Autophagy *8*, 1757–1768. https://doi.org/10.4161/auto.21994.

18. Halban, P.A., Polonsky, K.S., Bowden, D.W., Hawkins, M.A., Ling, C., Mather, K.J., Powers, A.C., Rhodes, C.J., Sussel, L., and Weir, G.C. (2014). beta-cell failure in type 2 diabetes: postulated mechanisms and prospects for prevention and treatment. Diabetes Care *37*, 1751–1758. https://doi.org/10.2337/dc14-0396.

19. Parker, E.D., Lin, J., Mahoney, T., Ume, N., Yang, G., Gabbay, R.A., ElSayed, N.A., and Bannuru, R.R. (2024). Economic Costs of Diabetes in the U.S. in 2022. Diabetes Care *47*, 26–43. https://doi.org/10.2337/dci23-0085.

20. Karam, J.H., Grodsky, G.M., Forsham, P.H., and McWilliams, N.B. (1963). Excessive insulin response to glucose in obese subjects as measured by immunochemical assay. Diabetes *12*, 197–204. https://doi.org/10.2337/diab.12.3.197.

21. Butler, A.E., Janson, J., Bonner-Weir, S., Ritzel, R., Rizza, R.A., and Butler, P.C. (2003). Beta-cell deficit and increased beta-cell apoptosis in humans with type 2 diabetes. Diabetes *52*, 102–110. https://doi.org/10.2337/diabetes.52.1.102.

22. Haythorne, E., Lloyd, M., Walsby-Tickle, J., Tarasov, A.I., Sandbrink, J., Portillo, I., Exposito, R.T., Sachse, G., Cyranka, M., Rohm, M., et al. (2022). Altered glycolysis triggers impaired mitochondrial metabolism and mTORC1 activation in diabetic beta-cells. Nat. Commun. *13*, 6754. https://doi.org/10.1038/s41467-022-34095-x.

23. Nagamatsu, S., Nakamichi, Y., Yamamura, C., Matsushima, S., Watanabe, T., Ozawa, S., Furukawa, H., and Ishida, H. (1999). Decreased expression of t-SNARE, syntaxin 1, and SNAP-25 in pancreatic beta-cells is involved in impaired insulin secretion from diabetic GK rat islets: restoration of decreased t-SNARE proteins improves impaired insulin secretion. Diabetes *48*, 2367–2373. https://doi.org/10.2337/diabetes.48.12.2367.

24. Laybutt, D.R., Preston, A.M., Åkerfeldt, M.C., Kench, J.G., Busch, A.K., Biankin, A.V., and Biden, T.J. (2007). Endoplasmic reticulum stress contributes to beta cell apoptosis in type 2 diabetes. Diabetologia *50*, 752–763. https://doi.org/10.1007/s00125-006-0590-z.

25. Rohli, K.E., Stubbe, N.J., Walker, E.M., Pearson, G.L., Soleimanpour, S.A., and Stephens, S.B. (2024). A metabolic redox relay supports ER proinsulin export in pancreatic islet beta cells. JCI Insight *9*, e178725. https://doi.org/10.1172/jci.insight.178725.

26. Silva, J.P., Köhler, M., Graff, C., Oldfors, A., Magnuson, M.A., Berggren, P.O., and Larsson, N.G. (2000). Impaired insulin secretion and beta-cell loss in tissue-specific knockout mice with mitochondrial diabetes. Nat. Genet. *26*, 336–340. https://doi.org/10.1038/81649.

27. Hein, M.Y., Peng, D., Todorova, V., McCarthy, F., Kim, K., Liu, C., Savy, L., Januel, C., Baltazar-Nunez, R., Sekhar, M., et al. (2025). Global organelle profiling reveals subcellular localization and remodeling at proteome scale. Cell *188*, 1137–1155.e20. https://doi.org/10.1016/j.cell.2024.11.028.

28. Davies, A.K., Itzhak, D.N., Edgar, J.R., Archuleta, T.L., Hirst, J., Jackson, L.P., Robinson, M.S., and Borner, G.H.H. (2018). AP-4 vesicles contribute to spatial control of autophagy via RUSC-dependent peripheral delivery of ATG9A. Nat. Commun. *9*, 3958. https://doi.org/10.1038/s41467-018-06172-7.

29. Itzhak, D.N., Tyanova, S., Cox, J., and Borner, G.H. (2016). Global, quantitative and dynamic mapping of protein subcellular localization. eLife *5*, e16950. https://doi.org/10.7554/eLife.16950.

30. Schessner, J.P., Albrecht, V., Davies, A.K., Sinitcyn, P., and Borner, G.H.H. (2023). Deep and fast label-free Dynamic Organellar Mapping. Nat. Commun. *14*, 5252. https://doi.org/10.1038/s41467-023-41000-7.

31. Christopher, J.A., Geladaki, A., Dawson, C.S., Vennard, O.L., and Lilley, K.S. (2022). Subcellular Transcriptomics and Proteomics: A Comparative Methods Review. Mol. Cell. Proteomics *21*, 100186. https://doi.org/10.1016/j.mcpro.2021.100186.

32. Crook, O.M., Davies, C.T.R., Breckels, L.M., Christopher, J.A., Gatto, L., Kirk, P.D.W., and Lilley, K.S. (2022). Inferring differential subcellular localisation in comparative spatial proteomics using BANDLE. Nat. Commun. *13*, 5948. https://doi.org/10.1038/s41467-022-33570-9.

33. Dunkley, T.P.J., Watson, R., Griffin, J.L., Dupree, P., and Lilley, K.S. (2004). Localization of organelle proteins by isotope tagging (LOPIT). Mol. Cell. Proteomics *3*, 1128–1134. https://doi.org/10.1074/mcp.T400009-MCP200.

34. Gatto, L., Breckels, L.M., Wieczorek, S., Burger, T., and Lilley, K.S. (2014). Mass-spectrometry-based spatial proteomics data analysis using pRoloc and pRolocdata. Bioinformatics *30*, 1322–1324. https://doi.org/10.1093/bioinformatics/btu013.

35. Gatto, L., Vizcaíno, J.A., Hermjakob, H., Huber, W., and Lilley, K.S. (2010). Organelle proteomics experimental designs and analysis. Proteomics *10*, 3957–3969. https://doi.org/10.1002/pmic.201000244.

36. Geladaki, A., Kočevar Britovšek, N., Breckels, L.M., Smith, T.S., Vennard, O.L., Mulvey, C.M., Crook, O.M., Gatto, L., and Lilley, K.S. (2019). Combining LOPIT with differential ultracentrifugation for high-resolution spatial proteomics. Nat. Commun. *10*, 331. https://doi.org/10.1038/s41467-018-08191-w.

37. Guérin, A., Strelau, K.M., Barylyuk, K., Wallbank, B.A., Berry, L., Crook, O.M., Lilley, K.S., Waller, R.F., and Striepen, B. (2023). Cryptosporidium uses multiple distinct secretory organelles to interact with and modify its host cell. Cell Host Microbe *31*, 650–664.e6. https://doi.org/10.1016/j.chom.2023.03.001.

38. Mulvey, C.M., Breckels, L.M., Crook, O.M., Sanders, D.J., Ribeiro, A.L.R., Geladaki, A., Christoforou, A., Britovšek, N.K., Hurrell, T., Deery, M.J., et al. (2021). Spatiotemporal proteomic profiling of the pro-inflammatory response to lipopolysaccharide in the THP-1 human leukaemia cell line. Nat. Commun. *12*, 5773. https://doi.org/10.1038/s41467-021-26000-9.

39. Villanueva, E., Smith, T., Pizzinga, M., Elzek, M., Queiroz, R.M.L., Harvey, R.F., Breckels, L.M., Crook, O.M., Monti, M., Dezi, V., et al. (2024). System-wide analysis of RNA and protein subcellular localization dynamics. Nat. Methods *21*, 60–71. https://doi.org/10.1038/s41592-023-02101-9.

40. Krahmer, N., Najafi, B., Schueder, F., Quagliarini, F., Steger, M., Seitz, S., Kasper, R., Salinas, F., Cox, J., Uhlenhaut, N.H., et al. (2018). Organellar Proteomics and Phospho-Proteomics Reveal Subcellular Reorganization in Diet-Induced Hepatic Steatosis. Dev. Cell *47*, 205–221.e7. https://doi.org/10.1016/j.devcel.2018.09.017.

41. Foster, L.J., de Hoog, C.L., Zhang, Y., Zhang, Y., Xie, X., Mootha, V.K., and Mann, M. (2006). A mammalian organelle map by protein correlation profiling. Cell *125*, 187–199. https://doi.org/10.1016/j.cell.2006.03.022.

42. Shapiro, A.M.J., Lakey, J.R.T., Ryan, E.A., Korbutt, G.S., Toth, E., Warnock, G.L., Kneteman, N.M., and Rajotte, R.V. (2000). Islet transplantation in seven patients with type 1 diabetes mellitus using a glucocorticoid-free immunosuppressive regimen. N. Engl. J. Med. *343*, 230–238. https://doi.org/10.1056/NEJM200007273430401.

43. Korbutt, G.S., Elliott, J.F., Ao, Z., Smith, D.K., Warnock, G.L., and Rajotte, R.V. (1996). Large scale isolation, growth, and function of porcine neonatal islet cells. J. Clin. Investig. *97*, 2119–2129. https://doi.org/10.1172/JCI118649.

44. Harb, G., and Korbutt, G.S. (2006). Effect of prolonged in vitro exposure to high glucose on neonatal porcine pancreatic islets. J. Endocrinol. *191*, 37–44. https://doi.org/10.1677/joe.1.06812.

45. Kim, S., Whitener, R.L., Peiris, H., Gu, X., Chang, C.A., Lam, J.Y., Camunas-Soler, J., Park, I., Bevacqua, R.J., Tellez, K., et al. (2020). Molecular and genetic regulation of pig pancreatic islet cell development. Development *147*, dev186213. https://doi.org/10.1242/dev.186213.

46. van Gurp, L., Fodoulian, L., Oropeza, D., Furuyama, K., Bru-Tari, E., Vu, A.N., Kaddis, J.S., Rodríguez, I., Thorel, F., and Herrera, P.L. (2022). Generation of human islet cell type-specific identity genesets. Nat. Commun. *13*, 2020. https://doi.org/10.1038/s41467-022-29588-8.

47. Ouyang, W., Winsnes, C.F., Hjelmare, M., Cesnik, A.J., Åkesson, L., Xu, H., Sullivan, D.P., Dai, S., Lan, J., Jinmo, P., et al. (2019). Analysis of the Human Protein Atlas Image Classification competition. Nat. Methods *16*, 1254–1261. https://doi.org/10.1038/s41592-019-0658-6.

48. Haas, D.T., Weindl, D., Kakimoto, P., Trautmann, E.M., Schessner, J.P., Mao, X., Gerl, M.J., Gerwien, M., Muller, T.D., Klose, C., Cheng, X., et al. (2026). C-COMPASS: a user-friendly neural network tool profiles cell compartments at protein and lipid levels. Nat. Methods *23*, 118–130. https://doi.org/10.1038/s41592-025-02880-3.

49. Uhlén, M., Fagerberg, L., Hallström, B.M., Lindskog, C., Oksvold, P., Mardinoglu, A., Sivertsson, Å., Kampf, C., Sjöstedt, E., Asplund, A., et al. (2015). Proteomics. Tissue-based map of the human proteome. Science *347*, 1260419. https://doi.org/10.1126/science.1260419.

50. Rorsman, P., and Ashcroft, F.M. (2018). Pancreatic beta-Cell Electrical Activity and Insulin Secretion: Of Mice and Men. Physiol. Rev. *98*, 117–214. https://doi.org/10.1152/physrev.00008.2017.

51. Ellis, C., Lyon, J.G., and Korbutt, G.S. (2016). Optimization and Scale-up Isolation and Culture of Neonatal Porcine Islets: Potential for Clinical Application. Cell Transplant. *25*, 539–547. https://doi.org/10.3727/096368915X689451.

52. Prentki, M., and Nolan, C.J. (2006). Islet beta cell failure in type 2 diabetes. J. Clin. Investig. *116*, 1802–1812. https://doi.org/10.1172/JCI29103.

53. Groenen, M.A.M., Archibald, A.L., Uenishi, H., Tuggle, C.K., Takeuchi, Y., Rothschild, M.F., Rogel-Gaillard, C., Park, C., Milan, D., Megens, H.J., et al. (2012). Analyses of pig genomes provide insight into porcine demography and evolution. Nature *491*, 393–398. https://doi.org/10.1038/nature11622.

54. Shafrir, E., Ziv, E., and Mosthaf, L. (1999). Nutritionally induced insulin resistance and receptor defect leading to beta-cell failure in animal models. Ann. N. Y. Acad. Sci. *892*, 223–246. https://doi.org/10.1111/j.1749-6632.1999.tb07798.x.

55. Dalbøge, L.S., Almholt, D.L.C., Neerup, T.S.R., Vassiliadis, E., Vrang, N., Pedersen, L., Fosgerau, K., and Jelsing, J. (2013). Characterisation of age-dependent beta cell dynamics in the male db/db mice. PLoS One *8*, e82813. https://doi.org/10.1371/journal.pone.0082813.

56. Motomura, K., Matsuzaka, T., Shichino, S., Ogawa, T., Pan, H., Nakajima, T., Asano, Y., Okayama, T., Takeuchi, T., Ohno, H., et al. (2024). Single-Cell Transcriptome Profiling of Pancreatic Islets From Early Diabetic Mice Identifies Anxa10 for Ca2+ Allostasis Toward beta-Cell Failure. Diabetes *73*, 75–92. https://doi.org/10.2337/db23-0212.

57. Wang, Q., and Brubaker, P. (2002). Glucagon-like peptide-1 treatment delays the onset of diabetes in 8 week-old db/db mice. Diabetologia *45*, 1263–1273. https://doi.org/10.1007/s00125-002-0828-3.

58. Zhang, Y., Han, S., Liu, C., Zheng, Y., Li, H., Gao, F., Bian, Y., Liu, X., Liu, H., Hu, S., et al. (2023). THADA inhibition in mice protects against type 2 diabetes mellitus by improving pancreatic beta-cell function and preserving beta-cell mass. Nat. Commun. *14*, 1020. https://doi.org/10.1038/s41467-023-36680-0.

59. Zhong, Y., Wang, J., Gu, P., Shao, J., Lu, B., and Jiang, S. (2012). Effect of ezetimibe on insulin secretion in db/db diabetic mice. Exp. Diabetes Res. *2012*, 1–6. https://doi.org/10.1155/2012/420854.

60. Costanzo, M.C., von Grotthuss, M., Massung, J., Jang, D., Caulkins, L., Koesterer, R., Gilbert, C., Welch, R.P., Kudtarkar, P., Hoang, Q., et al. (2023). The Type 2 Diabetes Knowledge Portal: An open access genetic resource dedicated to type 2 diabetes and related traits. Cell Metab. *35*, 695–710.e6. https://doi.org/10.1016/j.cmet.2023.03.001.

61. Lipson, K.L., Fonseca, S.G., Ishigaki, S., Nguyen, L.X., Foss, E., Bortell, R., Rossini, A.A., and Urano, F. (2006). Regulation of insulin biosynthesis in pancreatic beta cells by an endoplasmic reticulum-resident protein kinase IRE1. Cell Metab. *4*, 245–254. https://doi.org/10.1016/j.cmet.2006.07.007.

62. Oh, S.J., Park, K., Sonn, S.K., Oh, G.T., and Lee, M.S. (2023). Pancreatic beta-cell mitophagy as an adaptive response to metabolic stress and the underlying mechanism that involves lysosomal Ca(2+) release. Exp. Mol. Med. *55*, 1922–1932. https://doi.org/10.1038/s12276-023-01055-4.

63. Kulkarni, A., Muralidharan, C., May, S.C., Tersey, S.A., and Mirmira, R.G. (2022). Inside the beta Cell: Molecular Stress Response Pathways in Diabetes Pathogenesis. Endocrinology *164*, bqac184. https://doi.org/10.1210/endocr/bqac184.

64. Paul, A., Wilson, S., Belham, C.M., Robinson, C.J.M., Scott, P.H., Gould, G.W., and Plevin, R. (1997). Stress-activated protein kinases: activation, regulation and function. Cell. Signal. *9*, 403–410. https://doi.org/10.1016/s0898-6568(97)00042-9.

65. Huang, C.Y., Wu, Y.M., Hsu, C.Y., Lee, W.S., Lai, M.D., Lu, T.J., Huang, C.L., Leu, T.H., Shih, H.M., Fang, H.I., et al. (2002). Caspase activation of

mammalian sterile 20-like kinase 3 (Mst3). Nuclear translocation and induction of apoptosis. J. Biol. Chem. *277*, 34367–34374. https://doi.org/10.1074/jbc.M202468200.

66. Wolf, A., Beuerlein, K., Eckart, C., Weiser, H., Dickkopf, B., Müller, H., Sakurai, H., and Kracht, M. (2011). Identification and functional characterization of novel phosphorylation sites in TAK1-binding protein (TAB) 1. PLoS One *6*, e29256. https://doi.org/10.1371/journal.pone.0029256.

67. Rutter, G.A., Georgiadou, E., Martinez-Sanchez, A., and Pullen, T.J. (2020). Metabolic and functional specialisations of the pancreatic beta cell: gene disallowance, mitochondrial metabolism and intercellular connectivity. Diabetologia *63*, 1990–1998. https://doi.org/10.1007/s00125-020-05205-5.

68. Haythorne, E., Rohm, M., van de Bunt, M., Brereton, M.F., Tarasov, A.I., Blacker, T.S., Sachse, G., Silva Dos Santos, M., Terron Exposito, R., Davis, S., et al. (2019). Diabetes causes marked inhibition of mitochondrial metabolism in pancreatic beta-cells. Nat. Commun. *10*, 2474. https://doi.org/10.1038/s41467-019-10189-x.

69. Schworer, S., Berisa, M., Violante, S., Qin, W., Zhu, J., Hendrickson, R.C., Cross, J.R., and Thompson, C.B. (2020). Proline biosynthesis is a vent for TGFbeta-induced mitochondrial redox stress. EMBO J. *39*, e103334. https://doi.org/10.15252/embj.2019103334.

70. Liu, Z., Jeppesen, P.B., Gregersen, S., Bach Larsen, L., and Hermansen, K. (2016). Chronic Exposure to Proline Causes Aminoacidotoxicity and Impaired Beta-Cell Function: Studies In Vitro. Rev. Diabet. Stud. *13*, 66–78. https://doi.org/10.1900/RDS.2016.13.66.

71. Kolic, J., Sun, W.G., Cen, H.H., Ewald, J.D., Rogalski, J.C., Sasaki, S., Sun, H., Rajesh, V., Xia, Y.H., Moravcova, R., et al. (2024). Proteomic predictors of individualized nutrient-specific insulin secretion in health and disease. Cell Metab. *36*, 1619–1633.e5. https://doi.org/10.1016/j.cmet.2024.06.001.

72. Ewald, J.D., Lu, Y., Ellis, C.E., Worton, J., Kolic, J., Sasaki, S., Zhang, D., Dos Santos, T., Spigelman, A.F., Bautista, A., et al. (2025). HumanIslets.com: Improving accessibility, integration, and usability of human research islet data. Cell Metab. *37*, 7–11. https://doi.org/10.1016/j.cmet.2024.09.001.

73. Mitrakou, A., Kelley, D., Mokan, M., Veneman, T., Pangburn, T., Reilly, J., and Gerich, J. (1992). Role of reduced suppression of glucose production and diminished early insulin release in impaired glucose tolerance. N. Engl. J. Med. *326*, 22–29. https://doi.org/10.1056/NEJM199201023260104.

74. Omar-Hmeadi, M., and Idevall-Hagren, O. (2021). Insulin granule biogenesis and exocytosis. Cell. Mol. Life Sci. *78*, 1957–1970. https://doi.org/10.1007/s00018-020-03688-4.

75. Fu, J., Githaka, J.M., Dai, X., Plummer, G., Suzuki, K., Spigelman, A.F., Bautista, A., Kim, R., Greitzer-Antes, D., Fox, J.E.M., et al. (2019). A glucose-dependent spatial patterning of exocytosis in human beta-cells is disrupted in type 2 diabetes. JCI Insight *4*, e127896. https://doi.org/10.1172/jci.insight.127896.

76. Kang, T., Boland, B.B., Alarcon, C., Grimsby, J.S., Rhodes, C.J., and Larsen, M.R. (2019). Proteomic Analysis of Restored Insulin Production and Trafficking in Obese Diabetic Mouse Pancreatic Islets Following Euglycemia. J. Proteome Res. *18*, 3245–3258. https://doi.org/10.1021/acs.jproteome.9b00160.

77. Li, M., Feng, F., Feng, H., Hu, P., Xue, Y., Xu, T., and Song, E. (2022). VAMP4 regulates insulin levels by targeting secretory granules to lysosomes. J. Cell Biol. *221*, e202110164. https://doi.org/10.1083/jcb.202110164.

78. Jain, C., Lickert, H., Ansarullah, Bilekova, S., and Bilekova, S. (2022). Targeting pancreatic beta cells for diabetes treatment. Nat. Metab. *4*, 1097–1108. https://doi.org/10.1038/s42255-022-00618-5.

79. Naslavsky, N., and Caplan, S. (2011). EHD proteins: key conductors of endocytic transport. Trends Cell Biol. *21*, 122–131. https://doi.org/10.1016/j.tcb.2010.10.003.

80. Seaman, M.N.J., Marcusson, E.G., Cereghino, J.L., and Emr, S.D. (1997). Endosome to Golgi retrieval of the vacuolar protein sorting receptor, Vps10p, requires the function of the VPS29, VPS30, and VPS35 gene products. J. Cell Biol. *137*, 79–92. https://doi.org/10.1083/jcb.137.1.79.

81. Di Paolo, G., and De Camilli, P. (2006). Phosphoinositides in cell regulation and membrane dynamics. Nature *443*, 651–657. https://doi.org/10.1038/nature05185.

82. Rameh, L.E., and Deeney, J.T. (2016). Phosphoinositide signalling in type 2 diabetes: a beta-cell perspective. Biochem. Soc. Trans. *44*, 293–298. https://doi.org/10.1042/BST20150229.

83. Tomas, A., Yermen, B., Regazzi, R., Pessin, J.E., and Halban, P.A. (2010). Regulation of Insulin Secretion by Phosphatidylinositol-4,5-Bisphosphate. Traffic *11*, 123–137. https://doi.org/10.1111/j.1600-0854.2009.00996.x.

84. Nguyen, K.T.T., Tajmir, P., Lin, C.H., Liadis, N., Zhu, X.D., Eweida, M., Tolasa-Karaman, G., Cai, F., Wang, R., Kitamura, T., et al. (2006). Essential role of Pten in body size determination and pancreatic beta-cell homeostasis in vivo. Mol. Cell Biol. *26*, 4511–4518. https://doi.org/10.1128/MCB.00238-06.

85. Stiernet, P., Guiot, Y., Gilon, P., and Henquin, J.C. (2006). Glucose acutely decreases pH of secretory granules in mouse pancreatic islets. Mechanisms and influence on insulin secretion. J. Biol. Chem. *281*, 22142–22151. https://doi.org/10.1074/jbc.M513224200.

86. Rhodes, C.J., Lucas, C.A., Mutkoski, R.L., Orci, L., and Halban, P.A. (1987). Stimulation by ATP of proinsulin to insulin conversion in isolated rat pancreatic islet secretory granules. Association with the ATP-dependent proton pump. J. Biol. Chem. *262*, 10712–10717. https://doi.org/10.1016/s0021-9258(18)61022-1.

87. Wang, L., Wu, D., Robinson, C.V., Wu, H., and Fu, T.M. (2020). Structures of a Complete Human V-ATPase Reveal Mechanisms of Its Assembly. Mol. Cell *80*, 501–511.e3. https://doi.org/10.1016/j.molcel.2020.09.029.

88. Sava, I., Davis, L.J., Gray, S.R., Bright, N.A., and Luzio, J.P. (2024). Reversible assembly and disassembly of V-ATPase during the lysosome regeneration cycle. Mol. Biol. Cell *35*, ar63. https://doi.org/10.1091/mbc.E23-08-0322.

89. Neukam, M., Sala, P., Brunner, A.D., Ganß, K., Palladini, A., Grzybek, M., Topcheva, O., Vasiljević, J., Broichhagen, J., Johnsson, K., et al. (2024). Purification of time-resolved insulin granules reveals proteomic and lipidomic changes during granule aging. Cell Rep. *43*, 113836. https://doi.org/10.1016/j.celrep.2024.113836.

90. Brunner, Y., Couté, Y., Iezzi, M., Foti, M., Fukuda, M., Hochstrasser, D.F., Wollheim, C.B., and Sanchez, J.C. (2007). Proteomics analysis of insulin secretory granules. Mol. Cell. Proteomics *6*, 1007–1017. https://doi.org/10.1074/mcp.M600443-MCP200.

91. Norris, N., Yau, B., Famularo, C., Webster, H., Loudovaris, T., Thomas, H.E., Larance, M., Senior, A.M., and Kebede, M.A. (2024). Optimized Proteomic Analysis of Insulin Granules From MIN6 Cells Identifies Scamp3, a Novel Regulator of Insulin Secretion and Content. Diabetes *73*, 2045–2054. https://doi.org/10.2337/db24-0355.

92. Li, M., Du, W., Zhou, M., Zheng, L., Song, E., and Hou, J. (2018). Proteomic analysis of insulin secretory granules in INS-1 cells by protein correlation profiling. Biophys. Rep. *4*, 329–338. https://doi.org/10.1007/s41048-018-0061-3.

93. Khater, S.I., Dowidar, M.F., Abdel-Aziz, A.E., Khamis, T., Dahran, N., Al-qahtani, L.S., Metwally, M.M.M., Al-Hady Abd-Elrahamn, A.S., Alsieni, M., Alosaimi, M.E., et al. (2022). beta-Cell Autophagy Pathway and Endoplasmic Reticulum Stress Regulating-Role of Liposomal Curcumin in Experimental Diabetes Mellitus: A Molecular and Morphometric Study. Antioxidants *11*, 2400. https://doi.org/10.3390/antiox11122400.

94. Gerber, P.A., and Rutter, G.A. (2017). The Role of Oxidative Stress and Hypoxia in Pancreatic Beta-Cell Dysfunction in Diabetes Mellitus. Antioxid. Redox Signal. *26*, 501–518. https://doi.org/10.1089/ars.2016.6755.

95. Zechner, D., Knapp, N., Bobrowski, A., Radecke, T., Genz, B., and Vollmar, B. (2014). Diabetes increases pancreatic fibrosis during chronic inflammation. Exp. Biol. Med. *239*, 670–676. https://doi.org/10.1177/1535370214527890.

96. Lee, E., Ryu, G.R., Ko, S.H., Ahn, Y.B., and Song, K.H. (2017). A role of pancreatic stellate cells in islet fibrosis and beta-cell dysfunction in type 2 diabetes mellitus. Biochem. Biophys. Res. Commun. *485*, 328–334. https://doi.org/10.1016/j.bbrc.2017.02.082.

97. Waselle, L., Gerona, R.R.L., Vitale, N., Martin, T.F.J., Bader, M.F., and Regazzi, R. (2005). Role of phosphoinositide signaling in the control of insulin exocytosis. Mol. Endocrinol. *19*, 3097–3106. https://doi.org/10.1210/me.2004-0530.

98. Malek, M., Kielkowska, A., Chessa, T., Anderson, K.E., Barneda, D., Pir, P., Nakanishi, H., Eguchi, S., Koizumi, A., Sasaki, J., et al. (2017). PTEN Regulates PI(3,4)P(2) Signaling Downstream of Class I PI3K. Mol. Cell *68*, 566–580.e10. https://doi.org/10.1016/j.molcel.2017.09.024.

99. Omar-Hmeadi, M., Guček, A., and Barg, S. (2023). Local PI(4,5)P(2) signaling inhibits fusion pore expansion during exocytosis. Cell Rep. *42*, 112036. https://doi.org/10.1016/j.celrep.2023.112036.

100. Stahelin, R.V. (2009). Lipid binding domains: more than simple lipid effectors. J. Lipid Res. *50*, S299–S304. https://doi.org/10.1194/jlr.R800078-JLR200.

101. Lin, C.W., Yan, F., Shimamura, S., Barg, S., and Shyng, S.L. (2005). Membrane phosphoinositides control insulin secretion through their effects on ATP-sensitive K+ channel activity. Diabetes *54*, 2852–2858. https://doi.org/10.2337/diabetes.54.10.2852.

102. Alzamora, R., Al-Bataineh, M.M., Liu, W., Gong, F., Li, H., Thali, R.F., Joho-Auchli, Y., Brunisholz, R.A., Satlin, L.M., Neumann, D., et al. (2013). AMP-activated protein kinase regulates the vacuolar H+-ATPase via direct phosphorylation of the A subunit (ATP6V1A) in the kidney. Am. J. Physiol. Ren. Physiol. *305*, F943–F956. https://doi.org/10.1152/ajprenal.00303.2013.

103. Al-bataineh, M.M., Gong, F., Marciszyn, A.L., Myerburg, M.M., and Pastor-Soler, N.M. (2014). Regulation of proximal tubule vacuolar H(+)-ATPase by PKA and AMP-activated protein kinase. Am. J. Physiol. Ren. Physiol. *306*, F981–F995. https://doi.org/10.1152/ajprenal.00362.2013.

104. Louagie, E., Taylor, N.A., Flamez, D., Roebroek, A.J.M., Bright, N.A., Meulemans, S., Quintens, R., Herrera, P.L., Schuit, F., Van de Ven, W.J.M., and Creemers, J.W.M. (2008). Role of furin in granular acidification in the endocrine pancreas: identification of the V-ATPase subunit Ac45 as a candidate substrate. Proc. Natl. Acad. Sci. USA *105*, 12319–12324. https://doi.org/10.1073/pnas.0800340105.

105. Pasquier, A., Vivot, K., Erbs, E., Spiegelhalter, C., Zhang, Z., Aubert, V., Liu, Z., Senkara, M., Maillard, E., Pinget, M., et al. (2019). Lysosomal degradation of newly formed insulin granules contributes to beta cell failure in diabetes. Nat. Commun. *10*, 3312. https://doi.org/10.1038/s41467-019-11170-4.

106. Deutsch, E.W., Bandeira, N., Perez-Riverol, Y., Sharma, V., Carver, J.J., Mendoza, L., Kundu, D.J., Wang, S., Bandla, C., Kamatchinathan, S., et al. (2023). The ProteomeXchange consortium at 10 years: 2023 update. Nucleic Acids Res. *51*, D1539–D1548. https://doi.org/10.1093/nar/gkac1040.

107. Perez-Riverol, Y., Bandla, C., Kundu, D.J., Kamatchinathan, S., Bai, J., Hewapathirana, S., John, N.S., Prakash, A., Walzer, M., Wang, S., and Vizcaíno, J. (2025). The PRIDE database at 20 years: 2025 update. Nucleic Acids Res. *53*, D543–D553. https://doi.org/10.1093/nar/gkae1011.

108. Schindelin, J., Arganda-Carreras, I., Frise, E., Kaynig, V., Longair, M., Pietzsch, T., Preibisch, S., Rueden, C., Saalfeld, S., Schmid, B., et al. (2012). Fiji: an open-source platform for biological-image analysis. Nat. Methods *9*, 676–682. https://doi.org/10.1038/nmeth.2019.

109. Tyanova, S., Temu, T., Sinitcyn, P., Carlson, A., Hein, M.Y., Geiger, T., Mann, M., and Cox, J. (2016). The Perseus computational platform for comprehensive analysis of (prote)omics data. Nat. Methods *13*, 731–740. https://doi.org/10.1038/nmeth.3901.

110. R Core Team (2020). R: A language and environment for statistical computing. https://www.r-project.org/.

111. Baker, C.P., Bruderer, R., Abbott, J., Arthur, J.S.C., and Brenes, A.J. (2024). Optimizing Spectronaut Search Parameters to Improve Data Quality with Minimal Proteome Coverage Reductions in DIA Analyses of Heterogeneous Samples. J. Proteome Res. *23*, 1926–1936. https://doi.org/10.1021/acs.jproteome.3c00671.

112. Scharp, D.W., Arulmoli, J., Morgan, K., Sunshine, H., and Hao, E. (2019). Advances in Human Islet Processing: Manufacturing Steps to Achieve Predictable Islet Outcomes from Research Pancreases. OBM Transplant. *03*, 1–97. https://doi.org/10.21926/obm.transplant.1901052.

113. Bastidas-Ponce, A., Roscioni, S.S., Burtscher, I., Bader, E., Sterr, M., Bakhti, M., and Lickert, H. (2017). Foxa2 and Pdx1 cooperatively regulate postnatal maturation of pancreatic beta-cells. Mol. Metab. *6*, 524–534. https://doi.org/10.1016/j.molmet.2017.03.007.

114. Pilz, J., Gloddek, N., Lindheimer, F., Lindner, M.J., Puhr-Westerheide, D., Ümütlü, M., Cyran, C., Seidensticker, M., Lindner, R., Kraetzl, M., et al. (2024). Functional maturation and longitudinal imaging of intraportal neonatal porcine islet grafts in genetically diabetic pigs. Am. J. Transplant. *24*, 1395–1405. https://doi.org/10.1016/j.ajt.2024.02.026.

115. Jeon, J., Correa-Medina, M., Ricordi, C., Edlund, H., and Diez, J.A. (2009). Endocrine cell clustering during human pancreas development. J. Histochem. Cytochem. *57*, 811–824. https://doi.org/10.1369/jhc.2009.953307.

116. Kulak, N.A., Pichler, G., Paron, I., Nagaraj, N., and Mann, M. (2014). Minimal, encapsulated proteomic-sample processing applied to copy-number estimation in eukaryotic cells. Nat. Methods *11*, 319–324. https://doi.org/10.1038/nmeth.2834.

117. Ford, L., Kennedy, A.D., Goodman, K.D., Pappan, K.L., Evans, A.M., Miller, L.A.D., Wulff, J.E., Wiggs, B.R., Lennon, J.J., Elsea, S., and Toal, D.R. (2020). Precision of a Clinical Metabolomics Profiling Platform for Use in the Identification of Inborn Errors of Metabolism. J. Appl. Lab. Med. *5*, 342–356. https://doi.org/10.1093/jalm/jfz026.

118. Evans, A.M., Br, B., Liu, Q., Mitchell, M.W., Rj, R., Dai, H., Sj, S., DeHaven, C.D., and Lad, M. (2014). High Resolution Mass Spectrometry Improves Data Quantity and Quality as Compared to Unit Mass Resolution Mass Spectrometry in High- Throughput Profiling Metabolomics. Metabolomics *4*, 1–3.

119. Lundberg, E., and Uhlén, M. (2010). Creation of an antibody-based subcellular protein atlas. Proteomics *10*, 3984–3996. https://doi.org/10.1002/pmic.201000125.

STAR★METHODS

KEY RESOURCES TABLE

REAGENT or RESOURCE	SOURCE	IDENTIFIER
Antibodies		
ATP6V1C1	Atlas antibodies, Sweden	HPA023943; RRID:AB_1845197
NHLRC3	Bioss - Thermo Fisher Scientific, USA	bs-9333R
P4HB	Atlas antibodies, Sweden	HPA018884; RRID:AB_1854896
PGRMC1	Atlas antibodies, Sweden	HPA064724
Goat anti-Mouse IgG (H+L) Cross-Adsorbed Secondary Antibody, Cyanine3	Invitrogen, Thermo Fisher Scientific, USA	A10521
Goat anti-Rabbit IgG (Heavy chain) Superclonal™ Secondary Antibody, Alexa Fluor™ 647	Invitrogen, Thermo Fisher Scientific, USA	A27040; RRID:AB_2536101
FITC Mouse Anti-Glucagon	Novus Biologicals, USA	NBP2-21803F; RRID:AB_3266065
Alexa Fluor 647 Mouse Anti-Insulin	BD Bioscience, Germany	565689; RRID:AB_2739331
Biological samples		
Human Islets	Prodo Laboratories, USA	Human Islets for Research (HIR), Prodo Labs
Chemicals, peptides, and recombinant proteins		
DMEM GlutaMAX	Thermo Fisher Scientific, USA	31966021
0.5 M EDTA (pH 8.0)	Invitrogen, Thermo Fisher Scientific, USA	15575–038
2-Chloroacetamide	Sigma-Aldrich, Merck, Germany	C0267-100g
2-Propanol HPLC Grade 99,7+%	VWR, Germany	22906.K2
4,6-diamidino-2-phenylindole (DAPI; blue)	Thermo Fisher Scientific, USA	D1306
Acetonitril Hipersolv Chroma	VWR, Germany	20048320
Ammonia (NH_4OH) solution 25%	Fluka, Sigma-Aldrich, Merck, Germany	44273
Amphotericin	Thermo Fisher/Gibco	15290–026
Aprotinin	Sigma-Aldrich, Merck, Germany	A3428
BD Horizon™ Fixable Viability Stain 780	BD Pharmingen, Germany	565388
Bicinchoninic acid (BCA) assay	Thermo Fisher Scientific, USA	23225
BME vitamins	Sigma-Aldrich, Merck, Germany	B6891
Bond-Breaker TCEP Solution	Life Technologies, Thermo Fisher Scientific (USA)	77720
Bovine serum albumin	Sigma-Aldrich, Merck, Germany	A9418
BSA	Sigma-Aldrich, Merck, Germany	A1470
$CaCl_2$	Sigma-Aldrich, Merck, Germany	C7902
Cell culture H2O	BioWest, France	L0970-1000
Collagenase IV	Thermo Fisher Scientific, USA	17104019
Collagenase IV	Sigma-Aldrich, Merck, Germany	C9263
Collagenase P	Roche, Switzerland	11213865001
Collagenase V	Sigma-Aldrich, Merck, Germany	C9263
dPBS	Gibco, Thermo Fisher Scientific, USA	14190–094
Empore™ SDB-RPS Solid Phase Extraction Disks	3M, USA	2241
Ethyl acetate (EtOAc)	Merck, Germany	141-78-6
Fatty acid free BSA	Sigma-Aldrich, Merck, Germany	A8806
FBS	Thermo Fischer Scientific, USA	10270
Fixable Viability Stain 780	BD Bioscience, Germany	565388
Forskolin	Sigma-Aldrich, Merck, Germany	F3917

(*Continued on next page*)

Continued

REAGENT or RESOURCE	SOURCE	IDENTIFIER
Glucose	Sigma-Aldrich, Merck, Germany	G7021
Glutathione	Sigma-Aldrich, Merck, Germany	G6013
Ham's F10	Sigma-Aldrich, Merck, Germany	N6908
Ham's F12	Sigma-Aldrich, Merck, Germany	N3520
Hanks' balanced salt solution (HBSS)	Sigma-Aldrich, Merck, Germany; BioWest, France; Gibco, Thermo Fisher Scientific, USA	H6648, L0612-500, 14175-053
Heparin	Sigma-Aldrich, Merck, Germany	H3149
HEPES	Gibco, Thermo Fisher Scientific, USA	15630–056
ibidi Mounting Medium	Ibidi, Germany	50001
IBMX	Sigma-Aldrich, Merck, Germany	I5879
ITS supplement	Gibco, Thermo Fisher Scientific, USA	41400–045
Insulin	Sigma Aldrich, USA	I2018
L-glutamine	Sigma-Aldrich, Merck, Germany	G8540
Liraglutide	Novo Nordisk, Germany	Victoza 6 mg/mL
Lysyl EndopeptidaseR (Lys-C)	Wako, Japan	129–02541
Magnesium chloride ($MgCl_2$)	Sigma-Aldrich, Merck, Germany	M8266
Medium 199	Sigma-Aldrich, Merck, Germany	M4530
Methanol ROTISOLV®	Roth, Germany	HN41.1
Nicotinamide	Sigma-Aldrich, Merck, Germany	N0636
Optiprep	Sigma-Aldrich, Merck, Germany	D1556
Paraformaldehyd	Sigma-Aldrich, Merck, Germany	P6148
PBS	Thermo Fisher Scientific, USA	10010056
Pefabloc	Serva, Germany	31682.02
Pen Strep	Gibco, Thermo Fisher Scientific, USA	15140–122
Permeabilization Buffer 10X	ThermoFisher, Invitrogen, Germany	00-8333-56
Phosphatase inhibitor	Thermo Fischer Scientific, USA	A32957
PIM(3X)	Prodo Laboratories Inc, USA	PIM-3X001 GMP
PIM(ABS)	Prodo Laboratories Inc, USA	PIM-ABS001 GMP
PIM(G)	Prodo Laboratories Inc, USA	PIM-G001 GMP
PIM(S) Prodo islet media	Prodo Laboratories Inc, USA	PIM-S001 GMP
Potassium chloride (KCl)	Sigma-Aldrich, Merck, Germany	P9333
Potassium hydroxide (KOH)	Hach, USA	31425
Potassium phosphate monobasic (KH_2PO_4)	Sigma-Aldrich, Merck, Germany	P5379
Protease inhibitor	Thermo Fisher Scientific, USA	A32955
Retinoic acid	Tocris, Germany	695
RPMI 1640	Thermo Fisher Scientific, USA	21875034
Sodium deoxycholate (SDC)	Sigma-Aldrich, Merck, Germany	30970
Sodium palmitate	Sigma-Aldrich, Merck, Germany	P9767
Sucrose	Sigma-Aldrich, Merck, Germany	S9378
T3 analog	Tocris, Germany	5552
Trifluoroacetic acid for synthesis	Merck Millipore, Germany	8082600026
Tris-HCl	Roth, Germany	9090.3
Trolox TM	Sigma-Aldrich, Merck, Germany	238813
TrypLE™ Express Enzym	Gibco, Thermo Fisher Scientific, USA	12604013
Trypsin from porcine pancreas	Sigma-Aldrich, Merck, Germany	T6567
ULTIβ1®	Human Cell Design, France	UB1-100-BSA
ULTIβ1-BF®	Human Cell Design, France	UB1-100-NO_BSA
Zinc sulfate	Sigma-Aldrich, Merck, Germany	Z0251
β Mercaptoethanol	Gibco, Thermo Fisher Scientific, USA	21985–023

(*Continued on next page*)

Continued

REAGENT or RESOURCE	SOURCE	IDENTIFIER
βCOAT®	Human Cell Design, France	BC-120
Deposited data		
Proteomic raw data	PRIDE, Perez-Riverol et al.[107]	PXD064528
Experimental models: Cell lines		
EndoC-βH5®	Human Cell Design, France	BH5-WT-100
EndoC-βH5® GLTx	Human Cell Design, France	BH5-GLTx-350
Experimental models: Organisms/strains		
C57BLKS/J	Jackson Lab, USA	000662
C57BLKS/J db/db	Jackson Lab, USA	000642
German Landrace piglets	–	–
Software and algorithms		
GraphPad Prism	GraphPad Software, USA	Version v.9.5.1
C-COMPASS	Haas et al.[48]	Version 1
Fiji software	Schindelin et al.,[108]	N/A
Perseus	Tyanova et al.[109]	Version 1.6.15.0
R statistical computing environment	R. Core Team[110]	Version 4.0.2.R
Spectronaut	Biognosys AG, Schlieren, Switzerland[111]	Version 15.7.220308.50606

EXPERIMENTAL MODELS AND STUDY PARTICIPANT DETAILS

Mice

Experiments were performed in accordance with the Animal Protection Law of the European Union after permission by the Government of Upper Bavaria, Germany (License number TVA 23–173). Male C57BLKS/J and C57BLKS/J db/db mice were obtained from Jackson Laboratory, USA. They were housed in Helmholtz Zentrum München Animal Facility till the age of 8 weeks. Animals were housed in virus-antibody-free (VAF) facilities and kept in micro-isolated cages (3 mice per cage) with unrestricted access to autoclaved food and water. Mice were genotyped and body weight, and blood glucose was measured before islet isolation. Only male mice were used in this study; the influence of sex on the reported findings was not assessed. Each biological replicate represents a pool of islets from 5 male mice (n = 3 WT and n = 4 db/db for organelle proteomics; n = 7 WT and n = 12 db/db for metabolomics).

Human pancreatic islets

Human pancreatic islets were sourced from Prodo Laboratories following their published protocol.[112] Experiments were performed using islet preparations from non-diabetic cadaveric donors (Caucasian males). All samples tested negative for Gram stain and HIV. The islets were washed twice and resuspended with PIM(S) medium (Prodo laboratories PIM-S001GMP), supplemented with PIM(G) (Prodo laboratories, PIM-G001GMP), PIM(3X), and PIM(ABS) (PIM-ABS001GMP). After overnight incubation at 37°C, the islets were used for further experiments. No experimental groups were defined. Only pancreatic islets from male donors were used in this study; the influence of sex on the reported findings was not assessed. Each biological replicate represents islets from 1 donor (n = 3 for organelle proteomics; n = 7 for tissue proteomics, one sample was excluded due to technical problems).

Ethics statement

Human pancreatic islets were purchased from Prodo Laboratories, Inc. (Irvine, CA, USA). According to the supplier, donor pancreata were procured through authorized Organ Procurement Organizations under Institutional Review Board (IRB)-supervised protocols. Written informed consent for organ and tissue donation and research use was obtained from the donor or the donor's legally authorized representative prior to procurement. All samples were de-identified before receipt by the investigators. Prodo Laboratories complies with applicable U.S. regulations governing human tissue procurement and privacy protection (including HIPAA requirements) and states adherence to internationally recognized ethical principles, including the Declaration of Helsinki and the Convention on Human Rights and Biomedicine.

Pigs

Danish Large White x Pietrain cross piglets were housed in a farrowing pen together with the mother sow, and a heated nest were offered to the piglets. Sows had free access to water and were fed commercial feed. 3- to 5-day-old neonatal pigs were used as donors for islet isolation. For each replicate pancreatic islet material from 2 male and 2 females was pooled to leverage sex-specific

Sex	Age (years)	BMI	Reason of death	HbA1c (%)	Total proteome	Organelle profiling
male	32	26.9	Anoxic event	4.9	Yes	Yes
male	47	23.2	Head trauma	5.2	Yes	Yes
male	58	29.0	Stroke	5.0	Yes	Yes
male	41	28.5	Motor vehicle accident	5.3	Yes	No
male	35	24.25	Motor vehicle accident	5.4	Yes	No
male	37	25.38	Natural causes	5.5	Yes	No
male	47	33.24	Motor vehicle accident	5.2	Yes	No
male	25	26.6	Alleged Homicide	5.8	Yes	No

effects. With a total of $n = 4$ for organelle proteomics and $n = 8$ for tissue proteomics. All procedures were approved by the local authority of Upper Bavaria, Germany and were conducted in accordance with the German Animal Welfare Act, following the ARRIVE guidelines and Directive 2010/63/EU.

EndoC cells

EndoC-βH5 and EndoC-βH5 GLTx were directly obtained from Human Cell Design, France and not propagated. Authentication and mycoplasm testing were certified with delivery.

METHOD DETAILS

Pancreatic islet isolations

Mouse islet isolation

Islet isolation followed the protocol by Bastidas-Ponce et al.[113] The entire islet isolation was carried out on ice, unless otherwise stated. For each isolation from one animal, 8 mL of 15% Optiprep solution, 3 mL of G-Solution (HBSS, 1% (v/v) P/S, 1%(w/v) BSA, filtered), a syringe containing 2 mL Collagenase P, and an additional 15 mL Falcon tube with 1 mL Collagenase P were prepared on ice. The animal was exsanguinated via cervical dislocation, and the common bile duct near its junction with the small intestine was clamped. Collagenase P (G-Solution containing 0.1% (w/v) Collagenase P) was injected into the common bile duct at the duodenum (1–2 mL), after which the pancreas was transferred to the 15 mL Falcon tube containing 1 mL Collagenase P solution. The pancreas was digested at 37°C in a thermo-shaker (1,000 rpm, 7 min), followed by vigorous shaking for 5 s and incubation for another 7–8 min. The tubes were shaken again for 10 s and placed on ice. Digestion was halted by adding ice-cold G-Solution up to a final volume of 15 mL. The suspension was centrifuged at 1,000 rpm (214 G in an Eppendorf 5910R, S-4x Universal rotor) for 2 min, and the supernatant was discarded. The pellet was resuspended in 5 mL G-solution, centrifuged again under identical conditions, and this washing step was repeated once more. The final supernatant was removed, and the open tube was placed upside down on a paper towel for 2 s to remove excess liquid without drying the pellet. A discontinuous density gradient was created using different concentrations of Optiprep. Using a pipette boy set to minimal speed, 5.5 mL of 15% Optiprep (in RPMI) was gently added to each tube, and the pellet was resuspended carefully to avoid bubble formation. These 5.5 mL were transferred into a second Falcon tube containing 2.5 mL of pure 15% Optiprep (in RPMI) carefully to avoid disturbing the layer border. The original tube was washed with 6 mL G-solution, and the wash was gently layered to form the third phase. Three phases were clearly visible for all samples. The gradient was left at room temperature for 10 min to allow larger tissue fragments to settle before centrifugation at 1,700 rpm (617 G in an Eppendorf 5910R, S-4x Universal rotor) with acceleration set to 3 and deceleration set to 0. Cell strainers (70 μm, pre-wetted with G-solution) were placed on new 50 mL Falcon tubes. Islets were located in the fluffy interphase between the upper and middle layers. Approximately 5 mL of the upper layer was removed, and the interphase was aspirated with a 1 mL pipette and transferred onto the pre-wetted strainer. Islets were washed twice with 5 mL G-solution, then released by inverting the strainer over a suspension dish and rinsing with 5 mL G-solution. Islets were hand-picked under a light microscope using a pre-wetted 200-μL pipette and transferred into 5 cm suspension dishes, with around 100 islets per dish. The brown, round islets were inspected for morphology, washed with PBS, and lysed in lysis buffer (20% sucrose (w/v), 20 mM Tris-HCL pH 7.4, 0.5 mM EDTA pH 8.0, 5 mM KCl, 3 mM $MgCl_2$, protease and phosphatase inhibitors) using a glass homogenizer. For each organelle gradient, 150–200 islets from 5 mice were pooled yielding approximately 200 μg of protein per gradient. In the WT condition, three replicates corresponded to a total of 15 mice, whereas the db/db condition represented a total of 20 mice.

Pig islet isolation, maturation and characterization

3- to 5-day-old neonatal pigs were used as donors for islet isolation. Neonatal pig islet (NICC) isolation and culture was carried out as described previously.[114] Briefly, porcine pancreata were minced in Hanks' balanced salt solution (HBSS) supplemented with 0.25% BSA, 10 mmol/L HEPES, 100 U/ml penicillin and 0.1 mg/mL streptomycin, transferred to HBSS containing 2.5 mg/mL collagenase V, and incubated at 37°C for 16–18 min under gentle agitation. The digest was filtered, washed, and cultured in petri dishes containing recovery medium (1:1 mixture of Ham's F12 and medium 199, 0.5% BSA, 10 mmol/L glucose, 10 mmol/L L-glutamine, 10 mmol/L

HEPES, 10 mmol/L nicotinamide, 0.062% glutathione, 100 U/mL penicillin, 0.1 mg/mL streptomycin, 2.5 μg/mL amphotericin, 25 U/mL heparin, 0.5 mmol/L Pefabloc, 100 KIU aprotinin, 10 μmol/L Trolox, 1x BME vitamins, 15.2 μmol/L zinc sulfate, 1 μmol/L liraglutide, 1x ITS supplement) for two days, with full media change at day 1 after isolation. From day 3 ongoing, NICCs were cultured after full media change in Ham's F10 medium containing 10 mmol/L glucose, 0.5% BSA, 10 μmol/L IBMX, 10 mmol/L L-glutamine, 10 mmol/L nicotinamide, 1 μmol/L liraglutide, 100 U/ml penicillin and 0.1 mg/mL streptomycin, followed by half media change every other day. NICC cultures were done at 37°C in humidified air with 5% CO_2. Dynamic glucose-stimulated insulin secretion (dGSIS) of NICCs was performed at culture day 10 using the PERI4 perfusion system (Biorep Technologies). Prior dGSIS, NICCs were equilibrated in 3 mM glucose Krebs-Ringer-buffer-HEPES (KRBH; 137 mM NaCl, 5.36 mM KCl, 0.34 mM Na_2HPO_4, 0.81 mM $MgSO_4$, 4.17 mM $NaHCO_3$, 1.26 mM $CaCl_2$, 0.44 mM KH_2PO_4, 10 mM HEPES, 0.1% BSA, 3 mM glucose pH 7.35) at 37°C. After transferring NICCs into perfusion columns according to the manufacture's instruction, a 60-min flushing step with 3 mM glucose KRBH at a flow rate of 30 μL min−1 was performed. Subsequently, the perfusion protocols of 20 min KRBH 3 mM glucose, 20 min KRBH 16.7 mM glucose with 10 μM forskolin, 15 min KRBH 3 mM glucose, 20 min KRBH 16.7 mM glucose with 59.56 mM KCl and final 12 min KRBH 3 mM glucose were applied using a flow rate of 100 μL min−1 and sample collection in 96-well plates at 1-min intervals. After perfusion, NICCs were recovered from the columns and lysed for total insulin content measurement using 250 μL acid-ethanol (1.4% HCl (35%, vol/vol) in absolute ethanol), respectively. All samples were kept at −20°C until measured with an Insulin Ultrasensitive HTRF Assay Kit (62IN2PE, Cisbio/revvity). Secreted Beta cell and alpha cell contents in NICCs were evaluated by flow cytometry. Therefore, NICCs were first washed with PBS and then dissociated into single cells with TrypLE Express for 10–15 minutes at 37°C. After incubation with BD HorizonTM Fixable Viability Stain 780 for 30 min at 4°C and washing with PBS, cells were fixed in 4% PFA for 20 min at 4°C. After cell counting, 2×10^6 cells/sample were permeabilized and blocked using 100 μL of 5% serum in 1× permeabilization buffer and then incubated with primary antibodies at the appropriate concentration in the same buffer overnight at 4°C. Data were acquired using BD FACSAria III and analyzed using the FlowJo software. For organelle gradients 20% of individual preparations yielding ∼14,000 IEQ each were mixed from 4 animals (2 males and 2 females) resulting in 10,000–12,000 IEQ and 500 μg of protein. The pig organelle map was generated from 16 animals.

Cell culture

EndoC-βH5 or EndoC-βH5 GLTx cells (for glucolipotoxicity treatment) were cultured on freshly coated 8-well Ibidi chambers using βCoat (B-cell Biology Consortium, USA). βCoat aliquots were thawed on ice and diluted in cold DMEM (4.5 g/L glucose) supplemented with 1% Penicillin-Streptomycin. The coating solution was added to the wells, evenly distributed, and incubated at 37°C for 1 h. Just before seeding, the coating solution was removed, and 100,000 cells per well were seeded in Ultiβ1 medium. After 4 h, the medium was replaced with fresh Ultiβ1, and cell adhesion and morphology were monitored by microscopy. Plates were maintained at 37°C with 5% CO_2 in a humidified incubator. After 2 days of incubation, GLTx cell medium was replaced for 2 days with medium supplemented with 1.5 mM palmitate (fatty acid-free BSA conjugated, Palmitate:BSA molar ratio 5:1) and 30 mM glucose for glucolipotoxicity treatment. Control group (vehicle/BSA) medium was supplemented with fatty acid-free BSA solution.

Immunofluorescence

Cells were fixed with 4% paraformaldehyde (PFA) for 15 min at room temperature in a fume hood, then washed three times with PBS. Permeabilization was performed using 0.1% Triton X-100 in PBS for 10 min. Cells were blocked for 1 h at room temperature in blocking buffer (4% FBS in PBS or 5% BSA in PBS, depending on the primary antibody), followed by three PBS washes. Primary antibodies, diluted in 1% BSA in PBS buffer, were applied and incubated overnight at 4°C. The next day, cells were washed three times with PBS, and secondary antibodies (also diluted in 1% BSA in PBS buffer) were added for 1 h at room temperature. After a final series of three PBS washes (5 min each), cells were stored in Ibidi mounting medium at 4°C until imaging. Images were acquired with a confocal microscope (SP8, LEICA, Wetzler, Germany) with ×40 and ×63 objectives. Fiji software[115] was used for image analysis, with images being median projections of three confocal sections after background subtraction.

Organelle separation

Sucrose gradients were prepared following Krahmer et al. (2018).[40] Ultracentrifuge tubes (14 × 89 mm) were marked for volume, then filled with 6–7 mL of 20% sucrose solution (20% sucrose (w/v), 20 mM Tris-HCl (pH 7.4), 0.5 mM EDTA (pH = 8.0), 5 mM KCl, 3 mM $MgCl_2$), followed by the careful addition of 50% sucrose solution (50% sucrose (w/v), 20 mM Tris-HCl (pH 7.4), 0.5 mM EDTA (pH = 8.0), 5 mM KCl, 3 mM $MgCl_2$), beneath it using a syringe. The gradients were sealed, mixed using the BioComp Gradient Master 108, and stored at 4°C until use. For ultracentrifugation, gradient tubes and equipment were pre-cooled to 4°C. After removing 200 μL from the upper layer of the gradient, an equal volume of islet lysate was added along the tube wall. Centrifugation was performed at 100,000 g for 3 h at 4°C (Beckman Optima L-70, SW41 rotor). Post-centrifugation, 24 fractions were collected from each tube in 0.5 mL increments. Fractions 12–24 were diluted 1:1 with MilliQ water, followed by the addition of ethanol precipitation buffer (ethanol, 50 mM sodium acetate) (4:1 ratio) and storage at −20°C overnight.

Proteomics

Proteomics sample preparation

Proteomic sample preparation for LC-MS/MS analysis was performed as described previously[116] with minor adjustments. Proteins were precipitated with ethanol precipitation solution after overnight incubation, via centrifugation at 15,000 g for 15 min. The supernatant was discarded, and the remaining solvent was evaporated. Pellets were dissolved and lysed in SDC lysis buffer (2% SDC, 100 mM Tris-HCl pH 8.5) at 95°C for 10 min at 1,000 rpm, sonicated in high mode (30 s OFF, 30 s ON) for 10 cycles (Bioruptor Plus; Diagenode), protein concentration was determined by bicinchoninic acid (BCA) assay, and 25 μg of protein were collected for further analysis. Samples were incubated with TCEP and CAA (final concentrations of 10 mM and 40 mM, respectively) at 45°C for 10 min with 1,000-rpm shake without light exposure, and overnight digested (minimum 17 h) with trypsin and LysC (1:40, protease:protein ratio) at 37°C, 1,000 rpm shake. Subsequently, 2% TFA including MS grade isopropanol was added to samples with 1:1 volume-to-volume ratio to acidify the samples. Three layers of styrene divinylbenzene reversed-phase sulfonate (SDB-RPS; 3 M Empore) membranes were stacked to prepare custom-made StageTips which were used for desalting and purification of the acidified samples. StageTips membranes were activated with SDB-RPS pre-wash buffers (100% ACN, 1% TFA in 30% Methanol, 0.2% TFA, respectively) that were run through the membranes (centrifugation at 1,000 rpm for 5 min) subsequently. Following that, acidified samples were loaded on them, and the samples were centrifuged till dryness through the SDB-RPS membranes and washed by SDB-RPS wash buffers: EtOAc including 1% TFA, isopropanol including 1% TFA, and 0.2% TFA, respectively. Peptides elution from the membrane was done with 60-μL elution buffer (80% ACN, 1.25% NH_4OH) into PCR tubes and the buffer was evaporated by vacuum centrifuge (45 min at 45°C). Dried peptides were reconstituted in 6 μL of loading buffer (2% ACN, 0.1% TFA) and peptide concentration was estimated via optical measurement at 280 nm (Nanodrop 2000; Thermo Scientific). 500 ng of the samples were loaded onto 50 cm in-house packed HPLC column for LC-MS/MS analysis.

LC-MS/MS measurement and DIA settings

Peptide samples (0.5 μg) were analyzed using an EASY-nLC 1200 system connected to an Orbitrap Exploris 480 Mass Spectrometer with a nano-electrospray ion source. Peptides were separated on a 50 cm, 75 μm ID HPLC column packed with 1.9 μm C18 Reprosil particles at 60°C. FAIMS Pro was used with compensation voltages of −50 V and −70 V. A binary buffer system (buffer A: 0.1% formic acid; buffer B: 80% ACN in 0.1% formic acid) ran at 300 nL/min over a 60-min gradient (5–95% buffer B). Data-independent acquisition (DIA) mode was employed with a 2-s cycle time. Full MS scans covered a 300–1650 m/z range at 120,000 resolution, 45 ms injection time, and $3x10^6$ target ions. MS/MS scans, using HCD (30 NCE), achieved 15,000 resolution with 22 ms injection time and 1,000 target ions.

Human total tissue samples were measured on a TimsTOF HT mass spectrometer (Bruker) equipped with a CaptiveSpray 2 source online coupled to a Vanquish *Neo* HPLC (Thermo Scientific). Peptides were trapped on a nano-trap column (300-μm inner diameter (ID) × 5 mm, packed with Acclaim PepMap100 C18, 5μm, 100 Å from LC Packings) before separation by reversed-phase chromatography on the C18 analytical column (PepSep Advanced, 75μm ID × 250 mm, 1.5μm from Bruker) at 40°C. Peptides were eluted from the column at a flow of 250 nL/min using a nonlinear 45 min acetonitrile gradient from 3 to 40% in 0.1% formic acid. The DIA-Pasef method covered a mass range from 350 to 1,250 m/z and a mobility range from 0.65 to 1.35 1/ko, with a ramp and accumulation time of each 100ms. Precursor peptides were isolated using 34 variable MS/MS windows and 17 MS/MS ramps, resulting in an estimated cycle time of 1.91 s. Collision energy for 0.6 1/ko was set to 20 and for 1.6 1/ko to 59.

Metabolomics

Free amino acid profiling of isolated pancreatic islets was performed by Metabolon, Inc. (Durham, NC, USA) using a targeted liquid chromatography-tandem mass spectrometry (LC-MS/MS) platform.[117,118] Samples were prepared as dry pellets washed in PBS from isolated mouse pancreatic islets (approximately 160 islets per sample) and submitted to Metabolon for analysis. Following reconstitution, samples were analyzed for a panel of 22 amino acids and related metabolites. Analyte concentrations were determined against authenticated reference standards and reported in μg/mL, with corrected results expressed as μg per hundred islets based on sample-specific dilution factors (ranging from 0.087 to 0.286) and islet number. The lower limit of quantification (LLOQ) was analyte-dependent, with 0.25–1.0 μg/mL for amino acids; the upper limit of quantification (ULOQ) was 10–200 μg/mL. Analytes falling below the LLOQ were excluded from analysis (reported as BLOQ). Values flagged as above the limit of quantification (ALOQ) were retained as extrapolated estimates.

QUANTIFICATION AND STATISTICAL ANALYSIS

Statistics analysis

Randomization, blinding during data collection and analysis was not performed. For statistical analysis of all cellular experiments, normality and equal variances were formally tested using the D'Agostino-Pearson omnibus test. If the data did not follow normal (Gaussian) distribution, nonparametric analysis was performed as identified in the relevant Methods section. Analysis of the assays was performed using Microsoft Excel 2016, Perseus (version 1.6.15.0) and Prism (GraphPad Software, v.9.5.1). Enrichment analyses and Manhattan plots were visualized using ggplot package in the R statistical computing environment v.4.0.2.R. Figures were created with Adobe Illustrator and BioRender. For integration of genetic associations, HuGE scores from T2DKP[60] (23.11.2025) were used. Where statistical significance is presented as asterisks in figures, the following convention applies for FDR or *p* value: *<0.05, **<0.01;

***<0.001. The specific statistical test used is indicated in each relevant figure legend. Statistical details of experiments, including sample sizes (n), definitions of center and dispersion measures, and exact test used, are reported in the figure legends.

Proteome raw data processing

DIA raw files were processed using Spectronaut software (versions 18.6231227.55695 for gradients and mouse total proteome, and 19.0240606.62635 for human and pig total proteome, Copernicus, developed by Biognosys), employing directDIA analysis. The data was searched against the Uniprot human (homo sapiens) databases UP000005640_9606_2020 and UP000005640_9606_additional_2020, the Uniprot pig (sus scrofa) database UP000008227_9823, the Uniprot mouse (mus musculus) databases UP000000589_10090_2020 and UP000000589_10090_additional_2020. The standard processing parameters used were trypsin cleavage, allowing for a peptide length of 7–52 amino acids and up to two missed cleavages. Carbamidomethylation was set as a fixed modification, while methionine oxidation and N-terminal acetylation were set as variable modifications. Protein Quantification was performed by applying the MaxLFQ algorithm.

Proteome analysis

Perseus (version 1.6.15.0) was used for bioinformatics analysis, applying default settings unless specified otherwise. Prior to the analysis, filters were applied to remove common contaminants. Columns were annotated for GOBP, GOMF, GOCC, KEGG pathway, KEGG disease, and Corum names, Keywords, Uniprot function, Uniprot tissue specificity, Uniprot subcellular location, and for Uniprot disease terms by using Uniprot annotations mainAnnot.homo_sapiens_2021. LFQ values were converted to logarithmic scale (log2) and proteins were filtered for at least two valid measurements across biological replicates for any condition. Missing values were imputed using a normal distribution model (Gaussian normal distribution with a width of 0.3 and a downshift of 1.8). Differences in protein abundance between conditions were assessed using a two-sided student's *t* test. Significance was defined using a permutation-based false discovery rate (FDR <0.05) which estimates the empirical null distribution by random labeling of samples. The s_0-parameter controlling variance stabilization was set to 0, corresponding to an unmodified student's *t* test. Following normalization of median protein abundances from biological replicates using *Z* score, significant proteins were hierarchically clustered, employing Euclidean distance as a measure for row clustering. One-sided Fisher's exact tests utilized annotations from databases such as UniProtKB, Gene Ontology (GO), Kyoto Encyclopedia of Genes and Genomes (KEGG), and CORUM. Complete enrichment analysis results including *p*-values, FDRs, and significance scores are given in source files, representative selections are visualized in bubble plots.

C-COMPASS analysis

C-COMPASS[48] a software for PCP data analysis implemented in Python version 3.8.8. was used. Fractionation data were imported into C-COMPASS, with samples assigned to conditions, replicates, and fractions. Fractionation datasets were filtered to include proteins identified in at least two replicates per condition, with missing values replaced by zeros and profiles scaled to an area under the curve of one. Median profiles of replicates per condition were rescaled to a 0–1 range for visualization. Neural networks were trained with an organelle marker list derived from experimentally validated marker lists.[29,119] Markers from underrepresented compartments were upsampled. The batch size for upsampling was determined by the compartment with the most marker proteins, setting this as the standard. To enhance underrepresented marker batches, artificial profiles were created by calculating the median of three randomly selected marker profiles, adding noise based on twice the standard deviation of each fraction value, and re-scaling. Profiles representing two different compartments were merged and re-scaled to generate mixed profile batches with ratios of 25:75, 50:50, and 75:25.

Each biological replicate from the organelle separation process was independently processed through the neural networks. The input layer size was based on the number of fractions in each replicate dataset. The network included two hidden dense layers: the size of the first dense layer was optimized during hyperparameter tuning and varied from the number of classes plus 40%–60% of the difference between the input layer and the second dense layer size, with optimization steps of 2. The activation function for the first dense layer was ReLU, while the second layer used a linear activation function. A ReLU layer followed to ensure all output values were positive, and a normalization layer adjusted the values to sum to 1 across all neurons. The network's optimization involved randomly splitting the upsampled data, allocating 80% for training and 20% for validation, aiming to minimize the mean squared error. To prevent overfitting, an early stopping callback monitored validation loss with a patience of 5 epochs. Hyperparameters such as dense layer size, optimizer type (Adam, RMSprop, or SGD), and learning rate (ranging from 10^{-4} to 10^{-1} with logarithmic sampling) were tuned using the Keras Hyperband method, capped at 20 epochs and a reduction factor of 3.

The complete optimization procedure, comprising upsampling, profile mixing, training, and hyperparameter tuning, was executed in three rounds for each replicate dataset to determine the optimal neural network architecture. Once identified, the neural network was trained and applied to the entire dataset, including profiles with unknown localizations, repeated ten times to generate an ensemble results matrix. The final prediction values were averaged across all rounds and re-normalized to ensure that the class values summed to 1. Class Contribution (CC) values were calculated by averaging the neural network raw outputs from the ensemble and filtered with a threshold that covered 95% of the false positive values for each compartment. Values below this threshold were set to 0, and the prediction values across all compartments were re-normalized to sum to 1 per protein. Proteins that retained a single value greater than 1 after filtering were defined as having a single localization.

Each prediction was assigned to a specific compartment based on its highest CC value, or (before filtering) based on the highest neural network output. CC values were utilized for static localization statistics, and the difference in CC values across conditions provided the Relocalization (RL) values. Raw neural network outputs were used to calculate Cohen's Distance (D) per compartment, measuring the effect size and indicating the magnitude of differences between groups. The overall score Distance Score (DS) was determined by summing the absolute D values, while the Relocalization Score (RLS) was derived by summing the absolute RL values, filtering for relocalizations with RLS>1 and DS > 0.

Organelle modeling

For organelle-level clustering and quantification, all proteins with a non-zero organelle contribution (CC > 0) in at least one of the two conditions were retained. These proteins were intersected with the total proteome to ensure identical protein coverage across conditions. Differential abundance in the total islet proteome was assessed using a two-sided student's *t* test with permutation-based FDR correction (FDR<0.05). Proteins showing significant changes were *Z* score normalized across samples and subjected to supervised hierarchical clustering using Euclidean distance. Functional enrichment of clusters was evaluated against the organelle-resolved proteomes to identify compartment-specific functional changes.

Organelle quantification

Organelle abundance was quantified by summing the intensities of all marker proteins assigned to the indicated subcellular compartments. For each biological replicate the total intensity of compartment-specific markers was calculated. The average sum of intensities for the WT group was normalized to 1, and all individual values from both WT and db/db samples were normalized accordingly. A similar approach was used for the species-specific comparison. Here, summed marker intensities were compared to the overall sum of intensities across all compartments to obtain percentage values.

Insulin granule protein identification

To identify insulin granule-associated proteins within the protein correlation profiling (PCP) dataset, we applied a similarity-based statistical enrichment approach. A compartment-specific reference profile was generated by taking the median profile of 19 canonical insulin granule markers. For every protein, the Euclidean distance to this reference was computed as a continuous similarity metric, resulting in an empirical distance distribution for each species. Proteins with distances falling within the lowest 5% of this distribution (equivalent to the 95^{th} percentile similarity cutoff) were classified as significantly matching the insulin granule profile and annotated as putative insulin granule proteins.

Metabolomic data analysis

For between-sample normalization, corrected results (μg/100 islets) were additionally normalized to total protein content per sample. Statistical comparisons between db/db and wild-type groups were performed using the two-sided Mann-Whitney U test (*$p < 0.05$, **$p < 0.01$, ***$p < 0.001$).